Effects of Microstructure on the Susceptibility of Austenitic and Martensitic Stainless Steels to Pitting and Inter-granular Corrosion in Aqueous Chloride Environments

A Research Thesis
Presented to
The Academic Faculty

By

Tarun Vabhav Pratap Sikri

In Partial Fulfillment of the Requirements for the Degree
B.S. Materials Science and Engineering

Georgia Institute of Technology
Spring 2012

Georgia Institute of Technology

Effects of Microstructure on the Susceptibility of Austenitic and Martensitic Stainless Steels to Pitting and Inter-granular Corrosion in Aqueous Chloride Environments

May 4, 2012

Tarun Sikri 5/4/12

Tarun V.P. Sikri
Undergraduate Student
Materials Science and Engineering

5/4/12

Dr Preet M. Singh
Professor
Materials Science and Engineering

5/4/12

Dr Fred Cook
Associate Chair for Undergraduate Programs
Materials Science and Engineering

ACKNOWLEDGEMENTS

I would like to thank Sam Raji, Lindsey Goodman and Jamshad Mahmood for their patience and willingness to assist me with the microcell design and learning important laboratory techniques. Finally I would like to express my gratitude towards Professor Singh for his continued guidance in defining goals and completing this project.

TABLE OF CONTENTS

SUMMARY

Stainless steels are utilized for their high toughness and resistance to general corrosion. Austenitic (300 series) stainless steels are the most popular because they are ductile and can be easily formed into desired geometries. They can also be case hardened to form alternating layers of martensitic and austenitic microstructures for applications that require high toughness and resistance to surface wear. However their usage is limited in comparison to other ferrous alloys due to higher initial costs and susceptibility to pitting and intergranular (IGC) corrosion. A microcell was developed to study these localized corrosion phenomena in microstructural regions of interest by performing polarization (spot) tests within well defined areas on metallic surfaces. Spot tests across profiles of welded 304 stainless steel confirmed that sensitization, greater acidities and higher chloride contents increase susceptibility and greater additions of chromium and nickel reduce susceptibility to localized corrosion. Spot tests across a case hardened (CSS 42L) stainless steel profile revealed that the austenitic sensitized outer layer was more susceptible to localized attack compared to the martensitic matrix. A more complete understanding of how microstructure affects these localized corrosion processes will lead to better alloy modifications, service environments and maintenance making this class of material a more sustainable alternative.

CHAPTER 1 INTRODUCTION

In the chemical, petrochemical, food processing, construction and transportation industries where corrosion and high temperature oxidation are major concerns, stainless steels are ubiquitous due to their high toughness and resistance to general corrosion (Fig 1). Despite advancements in steel making technology these materials require a greater initial investment due to the high costs and low tolerances of alloying elements [1, 2]. The presence of a strongly adhering, several nanometer thick chromium oxide (passive) layer on the surface that limits reaction kinetics gives this class of material resistance to general corrosion and oxidation. However stainless steels are susceptible to various forms of localized attack in chloride-containing environments including: stress corrosion cracking (SCC), pitting corrosion, crevice corrosion and inter-granular corrosion (IGC). A fundamental understanding of how microstructure affects these mechanisms will allow modifications of alloy chemistry, plastic deformation, heat treatment, service environment and maintenance so that localized corrosion can be mitigated making this class of material a more sustainable alternative.

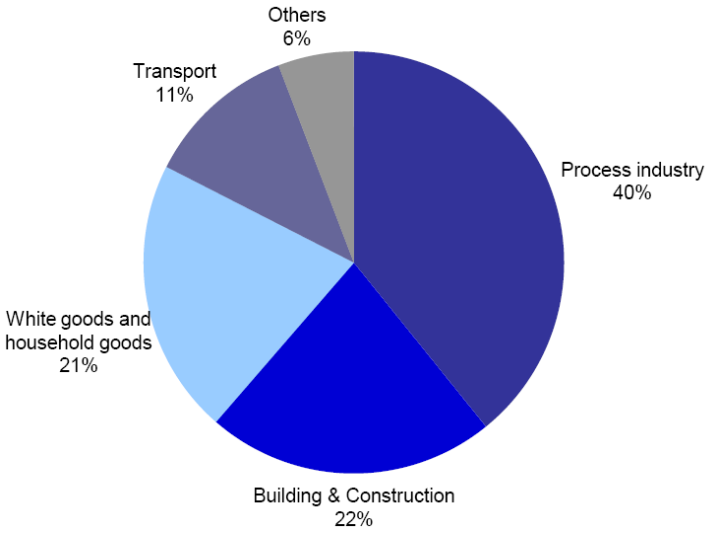

Figure 1: Percentage of stainless steel consumption by application in 2009; includes all grades [1].

1.1 Austenitic and Martensitic Stainless Steels

Austenitic chromium-nickel (300 series) stainless steels contain ratios of nickel to chromium alloying equivalents that stabilize the face centered cubic (FCC) phase at room temperature allowing for easy grain deformation corresponding to greater ductility and toughness values. Prolonged exposure at moderate temperatures (500 - 700^{o}C) promotes the precipitation of

chromium carbides at grain boundaries (sensitization) and the brittle sigma phase, these can be detrimental to mechanical performance and corrosion resistance. Nonetheless, due to a good combination of general corrosion resistance and desirable mechanical properties this group of alloys accounts for 70% of total US stainless steel production. Evaluating service conditions can optimize the specific alloy choice; minor compositional variations of type 304 (UNS S30400) comprise this specific alloy group (Fig 2) [2].

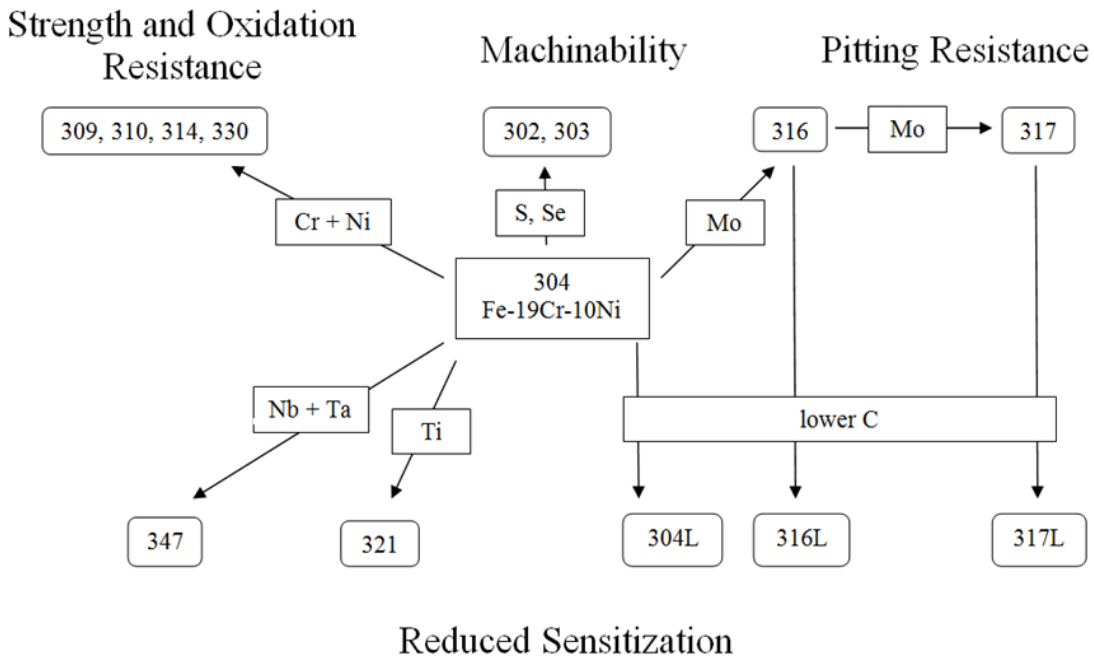

Figure 2: Compositional and property linkages in the family of austenitic chromium-nickel (300 series) stainless steel alloys, additions of niobium (Nb) and tantalum (Ta), titanium (Ti) and lowering carbon (C) content can reduce susceptibility to sensitization. Additions of chromium (Cr) and nickel (Ni) increase strength and resistance to oxidation, sulfur (S) additions make machining easier and additions of molybdenum (Mo) increase pitting resistance [2].

Rapid cooling (quenching) austenitic steels of certain compositions below a critical (Ms) temperature does not allow enough time for carbon to diffuse out of the more open FCC phase resulting in a hard, non-equilibrium martensite phase. This phenomena has been used to case-harden stainless steels for fabrication of gears and bearings requiring high surface hardness, core toughness and corrosion resistance [3].

1.2 Common Chloride Environments

Carbon steel reinforced concrete is a popular construction material due to its low cost and excellent compressive properties. However, the evolution of expansive iron oxides and hydroxides from corrosion of the steel reinforcement promotes subsequent spalling of the

surrounding concrete [4]. This spalling commonly occurs in concrete bridges and highways exposed to de-icing salts and aggressive marine environments, the annual direct costs associated with corrosion of highway bridges is estimated to be 8.3 billion USD [5]. Stainless steels have received increasing attention in recent years as a long-term, sustainable alternative to plain carbon steel for reinforced concrete [6, 7]. Ideally the highly alkaline and basic (pH ~13) concrete-pore solution surrounding steel embedded in concrete should form a stable passive film. However concrete porosity allows diffusion of ambient CO_2 and chlorides to the steel surface [8, 9] that promotes carbonation (Eq 1) increasing acidity (pH ~9) and initiating localized attack.

$$Ca(OH)_2 + CO_2 \rightarrow CaCO_3 + H_2O \quad (1)$$

Stainless steels comprising coastal buildings, desalination plants and crucial piping in offshore oil rigs are highly susceptible to localized corrosion due to the harsh marine environments [10]. These are characterized by nearly slightly basic (pH 7.0-8.0), aqueous solutions containing 1.94 weight % chlorides and high alkalinities due to the presence of carbonate salts [11, 12]. However service lives of stainless steel surfaces exposed to marine environments remain unpredictable even if alloy chemistries are accounted for (indicated by PREN value, see 2.2 *Pitting Corrosion*) [13].

1.3 Aqueous Corrosion Theory

Aqueous metallic corrosion is an electrochemical process that compromises metal oxidation (anodic) (Eq 2) and reduction (cathodic) reactions at the interface of a metal and aqueous electrolyte. Oxygen reduction (Eq 3) is observed in an aerated environment and hydrogen reduction (Eq 4) is observed in an acidic environment, both reduction reactions will occur in acidic, aerated environments.

$$M \rightarrow M^{n+} + ne^- \quad (2)$$

$$\frac{1}{2}O_2 + H_2O + 2e^- \rightarrow 2OH^- \quad (3)$$

$$2H^+ + 2e^- \rightarrow H_2(g) \quad (4)$$

Standard immersion tests are useful for predicting a given alloy's service life in some environments. However these require long testing times, are expensive and are unable to reveal fundamental chemical processes occurring at the surface.

1.4 Corrosion Testing: Cyclic Polarization

An anodic polarization test characterizes corrosion kinetics of a given alloy as a function of applied potential to the metallic surface (Fig 3a). Initially the sample surface (working electrode, WE) is allowed to equilibrate so that rates of anodic and cathodic reactions become equal giving a near-zero (exchange) current, this is measured as open circuit potential (OCP). Then a potentiostat gradually varies potential of the WE at a constant rate by using a feeback loop to monitor its instantaneous potential (Fig 3b). This allows a dynamic equilibrium to be achieved at each potential, the potential value corresponding to the exchange current changes from OCP to Ecorr because the surface is changed during the cathodic scan. Cathodic reactions dominate at potentials below Ecorr and anodic reactions dominate at potentials above Ecorr. A counter electrode (CE) provides an inert surface to support the necessary reactions so that an electrochemical circuit can be completed with the WE. All potentials are measured between the WE and reference electrode (RE); no reactions occur at the RE so that it can be relied upon as a stable reference. Absolute current measured during the cathodic scan is the difference between currents provided by cathodic and anodic reactions and the opposite is true for the anodic scan, current density (i) is found by normalizing measured current to test area. Reaction rates and activation energies for these competing processes can be found using Tafel extrapolation, this technique estimates linear slopes of potential versus current logarithm near Ecorr [14].

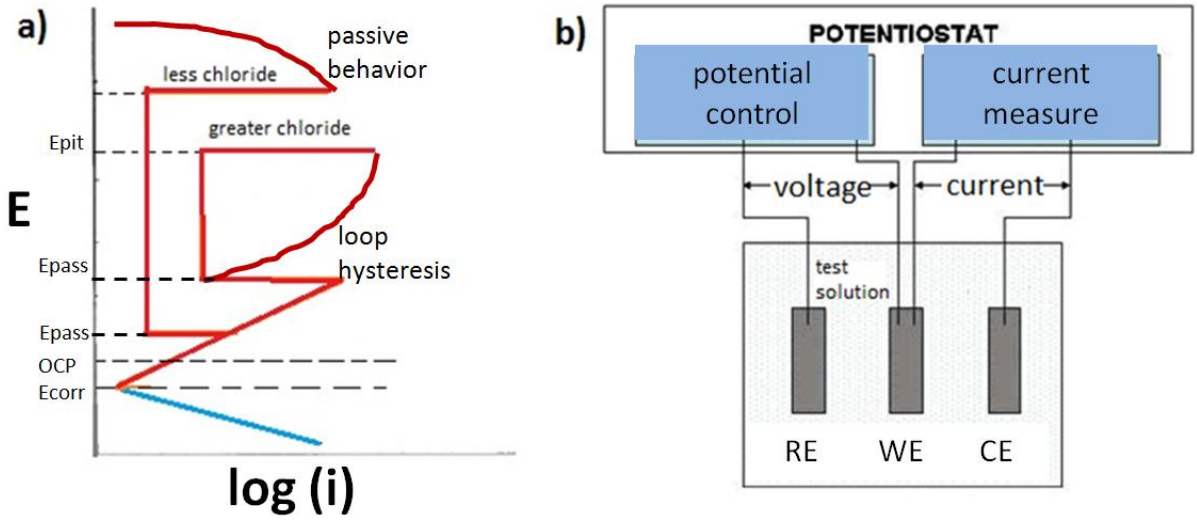

Figure 3: Cyclic polarization test (a) characterizes corrosion kinetics as a function of applied potential E, cathodic and anodic scans are shown as blue and red respectively, and the passive region is defined by the region of least current density during the forward anodic scan. Loop hysteresis during the reverse scan indicates localized damage to the passive film allowing greater current densities, lesser or similar current densities during the reverse scan indicate passive behavior. Greater chloride concentrations increase susceptibility to localized attack and show greater current densities during the anodic scan. A potentiostat (b) uses a feedback loop to control potential between RE and WE and measures current between WE and CE.

The reduced current density in the passive region is a direct consequence of reactant diffusion limited by the spontaneous oxide formation on the metal surface [15], increasing chloride concentration increases current density and Epass. Lesser or similar current densities after reversing (cyclic) anodic polarization indicate passive behavior. A loop hysteresis indicates localized damage to the passive film (pitting or crevice corrosion) increasing corrosion kinetics. Charge reacted per area (charge density, Q) can be found for any portion of the polarization scan by integrating current density with respect to time (t) (Eq 5).

$$Q = \int_{t1}^{t2} idt \tag{5}$$

This can be converted to mass reacted-per-area (m) (Eq 6) using Faraday's constant (F) 96,485.3 C/mol and equivalent weight (Z_{eq}).

$$m = \frac{\text{Zeq}}{F} * Q \tag{6}$$

This is found using known alloy composition (Eq 7) where variables fi, ni and ai correspond to weight fraction, common oxidation state and atomic weight of each element respectively [14].

$$\text{Z}_{\text{eq}} = \frac{1}{\sum_{\text{i}} \frac{\text{fi} * \text{ni}}{\text{ai}}} \tag{7}$$

CHAPTER 2 LITERATURE REVIEW

The ideal passive film on a stainless steel surface would prevent the occurrence of any type of corrosion. However certain microstructural features and environments diminish its effectiveness allowing localized attack to occur and research in recent decades has attempted to explain these processes.

2.1 Stainless Steel Passivity

Stainless steels contain a minimum of 11 weight % chromium that promotes instantaneous formation of a chromium-rich passive layer on a clean surface in ambient environments preventing general corrosion. However heat treatments and plastic deformation (cold/hot-working) result in chromium depletion and the introduction of non-protective oxides (scale), metallic particles, and other contaminants on the metal surface that hinder passivation [2]. Industrial methods utilize mechanical grinding and various acid treatments (pickling) that

remove scale and the chromium depleted layer so that ideal passivity can be restored; the specific pickling treatment depends on service expected environments [16, 17].

Studying passivity of stainless steel in an aqueous environment requires a model that is a state of dynamic equilibrium between film dissolution and growth [15] and is not yet fully understood. Electron spectroscopy for chemical analysis (ESCA) and ion etching techniques reveal similar passivation behaviors in atmosphere and aqueous chloride solution. These are characterized by a continuous transition from a hydrated outer layer, iron-chromium oxide middle layer, and metallic inner layer depleted in chromium and enriched in nickel [18]. Atomic force microscopy (AFM) and X-ray Photoelectron Spectroscopy (XPS) have revealed a smoother and more enriched passive film after treatment in nitric acid [19].

2.2 Pitting Corrosion

Pitting corrosion on a stainless steel surface is initiated by localized damage of the passive film due to mechanical wear or environmental aggressiveness; this allows local anodic dissolution of iron before the passive film is re-formed. Instantaneous re-passivation kinetics prevents a majority of the initiated (meta-stable) pits from developing into growing (stable) pits. If the local pit environment becomes depleted in dissolved oxygen relative to the surrounding metal, an area containing a small anode and large cathode and arises allowing stable pit growth governed by the following anodic (Eq 8) and cathodic (Eq 9) reactions.

$$Fe \rightarrow Fe^{2+} + 2e^{-} \tag{8}$$

$$\tfrac{1}{2}O_2 + H_2O + 2e^{-} \rightarrow 2OH^{-} \tag{9}$$

Iron dissolution is followed by hydrolysis (Eq 10) that deposits a salt film at the pit base; this is thought to play an important role in the kinetics of pit growth [15].

$$Fe^{2+} + 2H_2O \rightarrow Fe(OH)_2 + 2H^{+} \tag{10}$$

Migration of chloride anions to within the pit interior catalyzes the anodic and hydrolysis reactions which increase local pit acidity allowing additional hydrogen reduction (Eq 4) that accelerates localized attack. The different oxidizing tendencies of solution within and adjacent to the pit create an electrical potential difference allowing electron flow between the cathodic and anodic sites thereby completing the electrochemical circuit (Fig 4) [2].

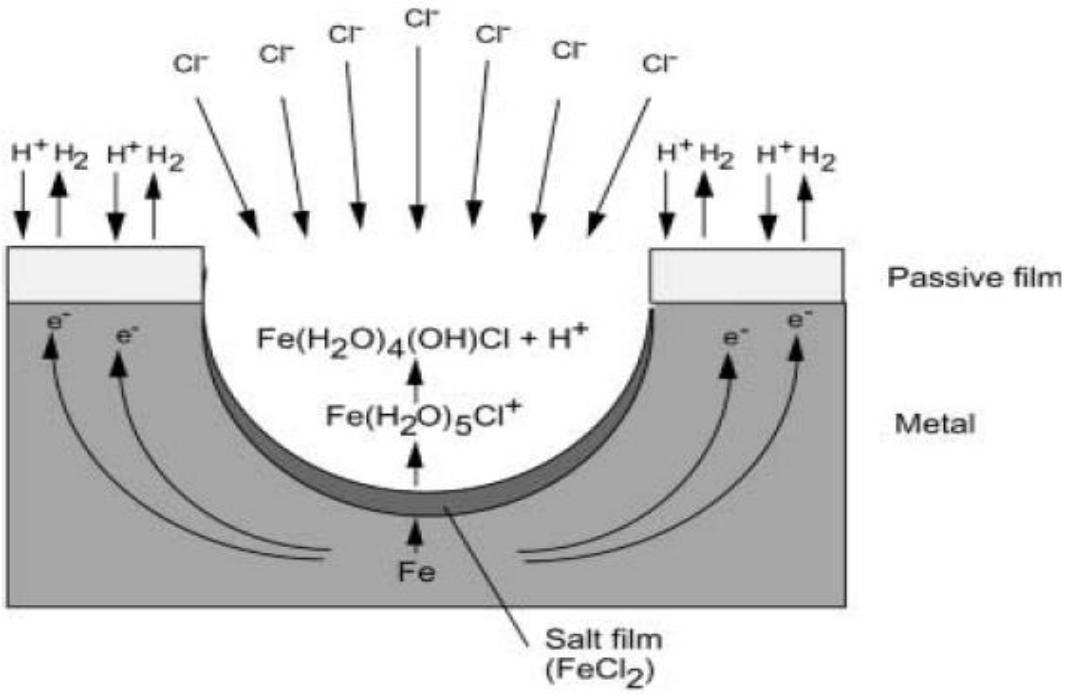

Figure 4: A stable pit showing iron oxidation within and hydrogen reduction adjacent to the pit, the voltage difference between these two sites allows electron flow completing the electrochemical circuit. Migration of chlorine into the pit promotes deposition of a salt film ($FeCl_2$ and $Fe(OH)_2$) at the pit base catalyzing the process [15].

Electrochemical tests and passive film analysis have revealed the presence chloride ions within the film only if the applied potential is above Epit indicating chloride ions initiate local breakdown of the passive film [20]. Chromium, molybdenum and nitrogen additions allow a pitting resistance equivalent number (PREN) to be calculated (Eq 11) and help determine if a particular alloy composition is suitable for a particular environment however it does not account for microstructure [2].

$$PREN = \%Cr + 3.3(\%Mo) + 16(\%N) \quad (11)$$

Electrochemical tests and passive film analysis have revealed that nitrogen and molybdenum have apparent synergistic effect that improves resistance to localized corrosion [21, 22]. Studies by Olefjord and Wegrlius indicate that the presence of nitrogen can lower local pit acidity (Eq 12-13) [23]; studies by Fu and Wu others have revealed that cold-working high-nitrogen stainless steels has no affect on pitting behavior [24].

$$N + 3H^+ + 3e^- \rightarrow NH_3 \quad (12)$$

$$N + 4H^+ + 3e^- \rightarrow NH_4^+ \quad (13)$$

2.3 *Intergranular Corrosion*

Intergranular Corrosion (IGC) is the preferred attack on chromium depleted zones adjacent to grain boundaries most commonly occurring in sensitized stainless steels and is typically observed after initial pit formation. Sensitizing stainless steels results in the evolution of chromium carbides at grain boundaries creating an adjacent chromium depleted zone due to slower diffusion of the larger chromium atoms (Fig 5a). A reduced passive film over these areas creates a small anode to cathode area ratio, allowing IGC ultimately leading to individual grains dislodging from the matrix [2]. Stainless steel parts joined by welding develop a sensitized region between the deposited weld and base metals that is especially prone to IGC (Fig 5b) [14] thereby requiring many industries to perform ASTM standardized-acid exposure tests prior to service.

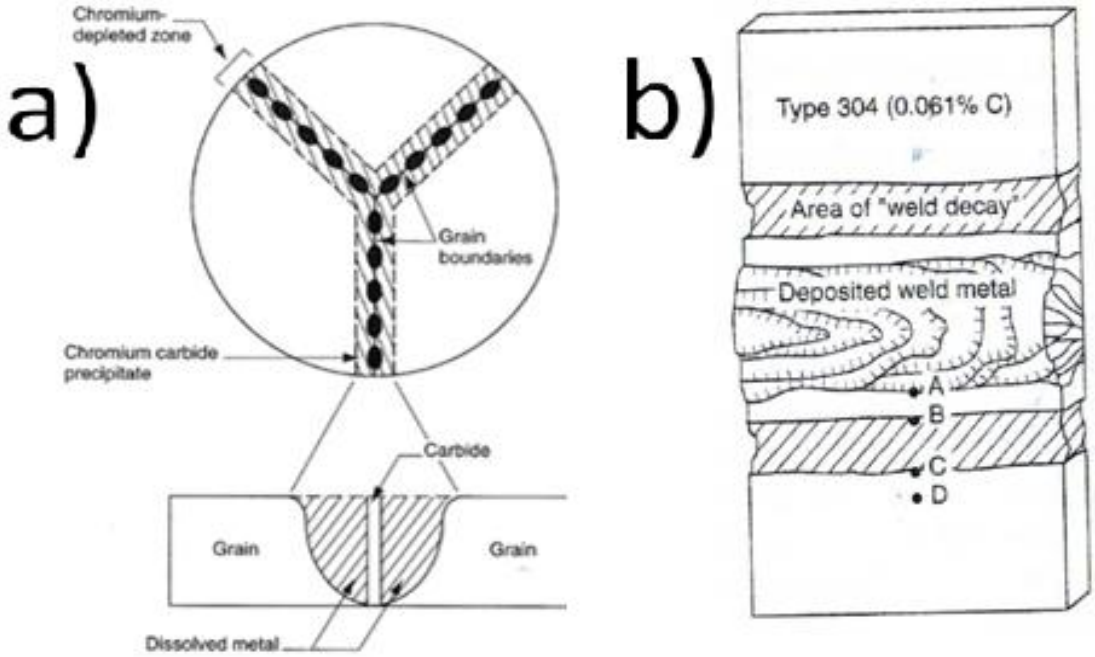

Figure 5: Heating stainless steels promotes sensitization resulting in chromium-depleted zones adjacent to grain boundaries (a) that are highly susceptible to IGC. Welding type 304 stainless steel (b) promotes sensitization (B and D) between the deposited weld (A) and base (D) metals [14].

Stainless steels alloyed with less carbon or strong carbide formers (titanium or niobium plus tantalum) are used as alternatives to prevent sensitization if welding is necessary (Fig 2) because subsequent solution annealing is often impractical [2].

2.4 Evaluating Localized Corrosion

Though useful for understanding general corrosion conventional large area (bulk) polarization tests are inadequate for understanding how certain microstructural features allow localized corrosion. Atomic Force Microscope (AFM) maps surface topography by measuring laser deflections from a cantilever moving across a corroding surface in raster fashion. A Kelvin probe measures corrosion potential as a function of position on the sample surface. Scanning reference electrodes (SRET) and scanning vibrating electrodes (SVET) measure corrosion current as a function of position on the sample surface. These techniques identify local anodic and cathodic sites however they require complex electronics and are limited to small, flat metallic samples [25]. A simple microcell developed by Bohni and Suter confines electrochemical activity on a metal surface to small areas ($< 50\ \mu^2$). This has allowed determination of corrosion susceptibility for distinct microstructural features of interest using polarization tests [26].

CHAPTER 3 MICROCELL DEVELOPMENT AND TECHNIQUE

A capillary would provide an electrochemical connection between the microcell body and a small area on the sample surface. The microcell was assembled from components of an optics board (Thor Labs) permitting greater freedom in sample stage assembly compared to attachment on an optical microscope [see proposal]. This would allow small area-corrosion testing to be performed on larger metallic objects while varying temperature and mechanical stresses.

3.1 Capillary Sealing

Polydimethyl silicone (PDMS) was found to be an appropriate polymeric material that could contain electrochemical activity within a well defined area. A particular type of PDMS (Cyclo C-953) that is filler free and polymerizes (cures) in the presence in of ambient moisture was found to work best (Table 1). Additionally it is hydrophobic, adheres strongly to glass surfaces and is resistant to acidic, basic and neutral aqueous solutions. However it is not dissolved by any common solvents so that once applied it can only be removed mechanically. The material was purchased in 85 gram tubes and stored in a vacuum chamber to limit contact with ambient moisture increasing its shelf life [27].

Table 1: The before and after cure properties of PDMS (Cyclo C-953) used for creating a capillary sealing that would contain electrochemical activity on a metallic surface [27].

cost (USD/oz)	0.80
uncured viscosity (cP)	5×10^4
skin time (min)	5
cure time (hrs)	24
ductility (%)	400
long term deformation (20-100^{o}C, %)	<5
resistivity (Ω-m)	$1x10^{15}$
hardness (durometer shore A)	25

Sealing formation at the end of a 6.35 mm diameter thick-walled capillary tube was based on a technique developed by Suter and Bohni [26]. Approximately 3 grams of PDMS were transferred to a disposable syringe for easy dispensing, and a glass capillary 4 cm long was cut from a larger glass tube using a sharp piece of ceramic. Both ends were rough polished with silicon carbide (SiC) sandpaper to create flat surfaces, one end was fine polished using water and 2000 grit SiC sandpaper. After drying, this end was covered with a thin PDMS coating and another syringe was used to force ethanol through its inner diameter so that excess PDMS could be removed to open a hole; this technique was repeated several times in 5 minute intervals. After achieving a 0.3 mm thickness the capillary sealing was gently rubbed on a polished metal surface covered with emulsified soap and water to smoothen it. Thin applications of PDMS, forcing ethanol through and gentle smoothening were repeated in 5 minute intervals until the sealing thickness was equal to half the capillary inner diameter; this was verified using an optical microscope. After waiting for the PDMS to fully cure compression tests using an optical microscope (Fig 6a) were used to verify sealing integrity and estimate hole size (Fig 6 b-c).

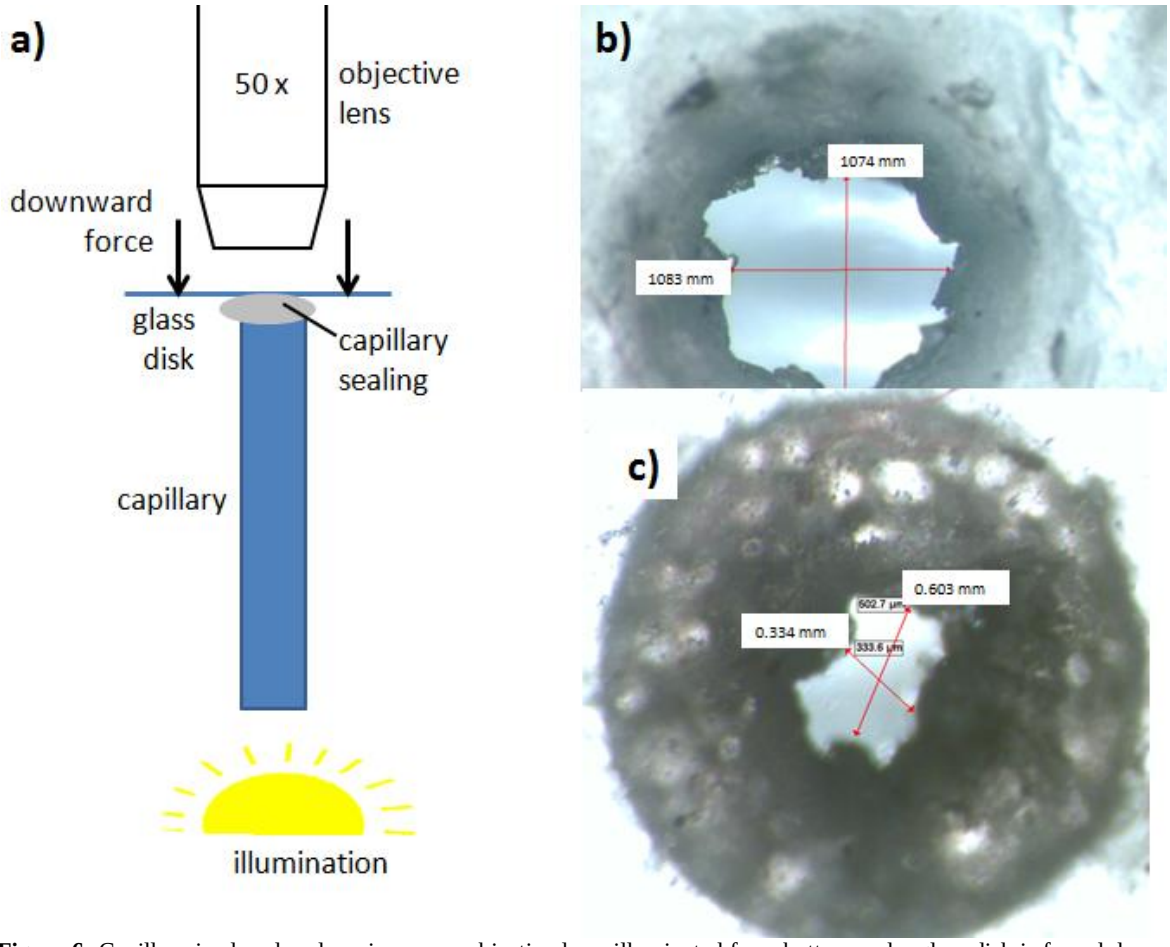

Figure 6: Capillary is placed under microscope objective lens, illuminated from bottom and a glass disk is forced downward on the capillary sealing (a) to verify its integrity and hole size before (b) and after compression (c).

3.2 Microcell Development

The microcell body was machined from a cube of clear acrylic plastic; a hole was drilled and tapped through five faces of the cube forming a central cavity. Each hole was fitted with the appropriate size Teflon fitting to form ports for the inlet tube, capillary, CE and RE.

Microcell 1.1 was assembled by clamping the microcell cube onto a Z-coarse adjust connected to a Z-clamp on the support column (Fig 7a), the sample was moved using X/Y adjusts. A platinum decal was adhered to a glass rod to fabricate the CE and the RE was fabricated from a glass tube containing a silver wire with silver chloride coating (Ag/AgCl) submerged in saturated KCl. This design was able to confine electrochemical activity to within a small area on the metal surface however it was difficult to assemble, maintain stable OCP and obtain reproducible results. Uncontrollable leaking at the capillary sealing (tip), misalignment of

the capillary relative to the sample surface normal (Fig 7b), unwanted sample movements during tests and poorly built RE and CE caused these problems.

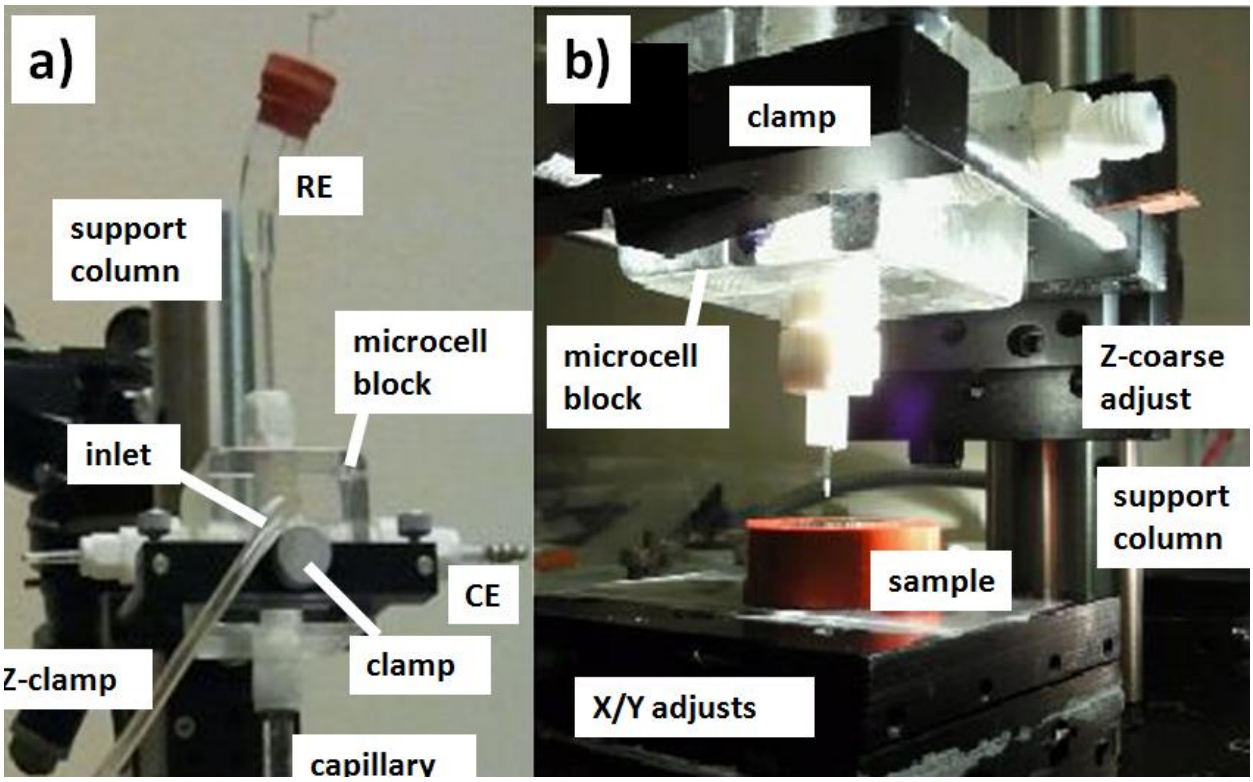

Figure 7: Reproducible data was difficult to obtain from Microcell 1.1 because of poorly built RE and CE (a) and misalignment of capillary relative to sample surface normal (b). A clamp secured the microcell cube to the Z-coarse adjust which was connected to a Z-clamp (not shown) on the support column.

Microcell 1.2 was assembled using rubber bands to secure the cube into bottom and back rubber supports (Fig 8a) improving capillary alignment normal to the sample surface. A new, extendable RE was fabricated from inner and outer glass tubes (Fig 8b) and a porous vycor frit served as a salt bridge between the saturated KCl in the RE body and test solution in the microcell cavity. The silver wire was secured through a rubber septum using tape so that the portion with a silver chloride coating would remain in the saturated KCl solution. A new CE was fabricated from a 0.5 mm diameter gold wire encapsulated in inner and outer glass tubes using PDMS (Fig 8c). This version allowed for an easier assembly, more stable OCP and reproducible data; however unwanted sample movements and uncontrollable leaking at the capillary tip remained a problem.

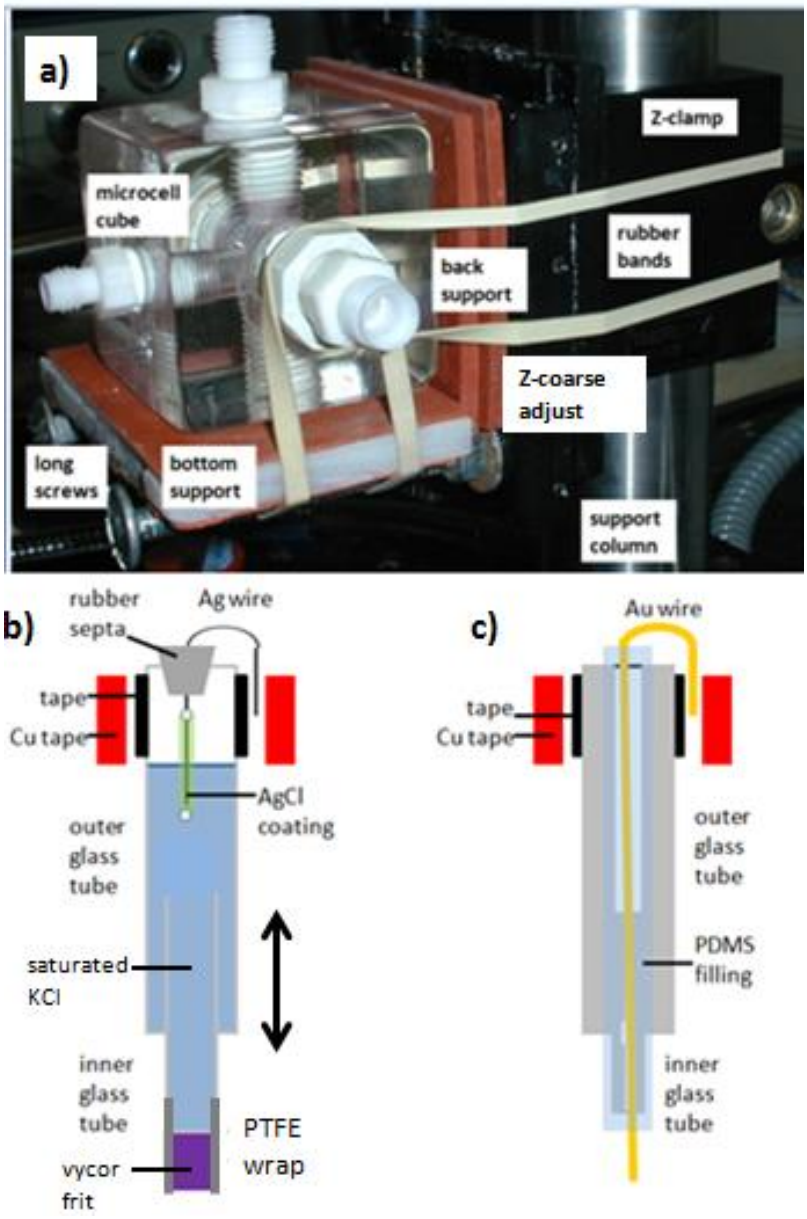

Figure 8: Rubber bands secured Microcell 1.2 into a right angle formed by bottom and back support (a) improving capillary alignment relative to the sample surface normal. An extendable RE was fabricated from inner and outer glass tubes (b), tape secured the Ag wire in a rubber septum so that the AgCl coating would remain in saturated KCl to provide a stable reference potential, and heat-shrinking a PTFE wrap attached the porous vycor frit to the end of the inner glass tube. A new CE was fabricated by encapsulating a 0.5 mm diameter gold wire inside inner and outer glass tubes using PDMS (c).

The presence of a positive air pressure within the microcell cavity was determined to be the cause of uncontrollable leaking at the capillary tip, and leak tests revealed sources of air percolation (Fig 9a). Teflon fittings were loosened from the microcell body, wrapped in Teflon tape and carefully re-fitted into the microcell body to form an airtight Microcell 1.3. This prevented uncontrollable leaking and allowed greater control of solution bubble at the capillary tip using a 1.0 mL syringe (Fig 9b). A sample stage was created to prevent unwanted motions

and provide electrically isolated connections to leads from the potentiostat. However frequent breakage of rubber bands and a lack of precise control of sealing compression at capillary-sample interface continued to be problems.

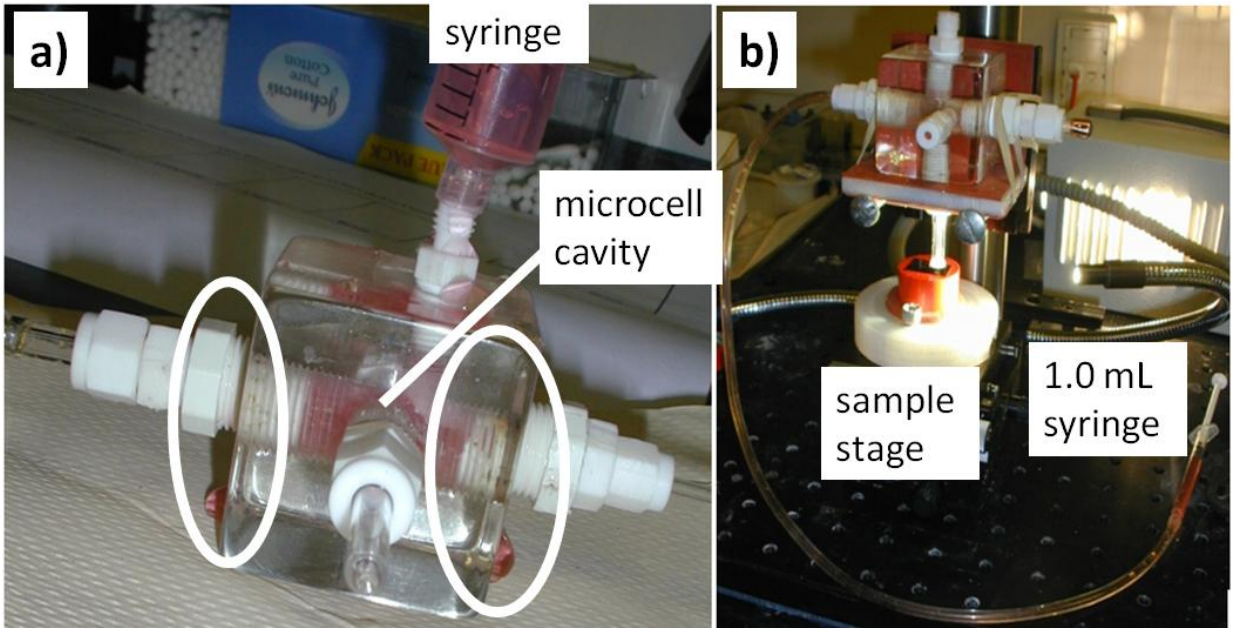

Figure 9: Leak tests pressurized the microcell cavity using a syringe with red-dyed solution to reveal sources of air percolation (circled) around Teflon fittings (a). Eliminating these air leaks reduced positive pressure within the cavity to create Microcell 1.3 allowing precise control of solution bubble at the capillary tip using a 1.0 mL syringe (b).

After attempting various configurations the best ports were finalized for the inlet, capillary, CE and RE, an extra X port remained since the cube was originally designed to be mounted onto an optical microscope (Fig 10a). A new sample stage was fabricated from a cut sheet of polypropylene plastic so that the sample surface would be more parallel to the XY plane. The Z-coarse adjust was replaced with a Z-fine adjust and rubber bands were replaced with elastic cords to create Microcell 1.4 (Fig 10b).

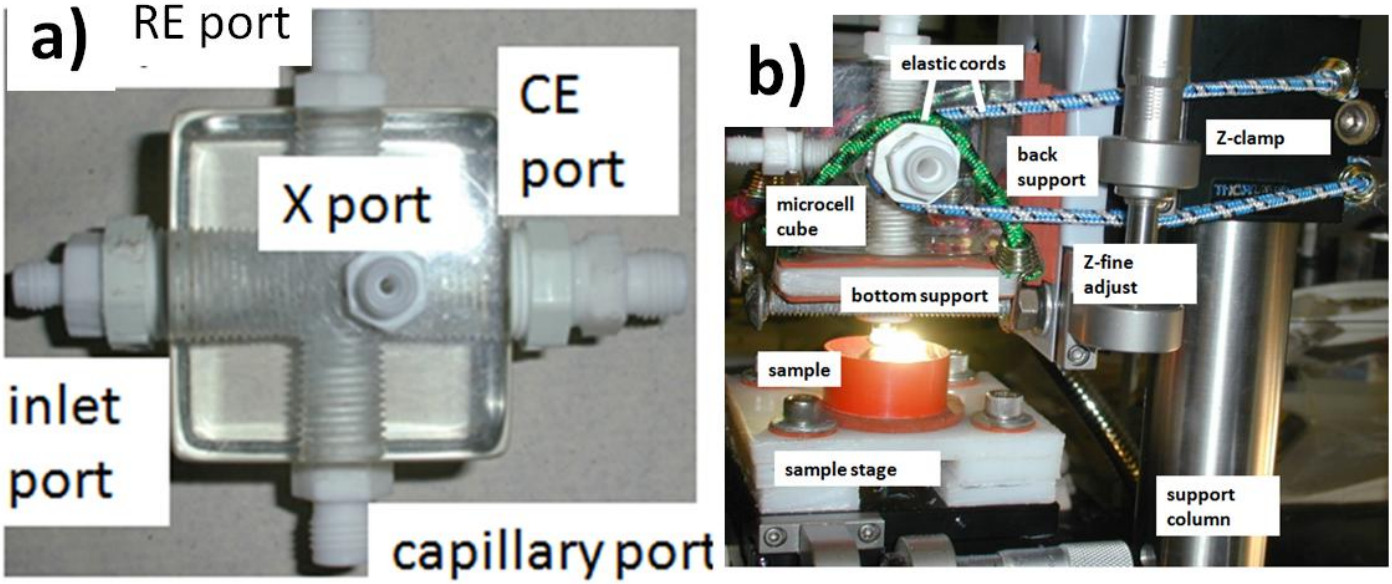

Figure 10: Ports on the microcell cube were finalized for the CE, RE, inlet and capillary, an extra X port remained since the cube was originally designed to be mounted onto an optical microscope. Microcells 1.4 shown with a new sample stage and microcell cube secured to Z-fine adjust using elastic cords.

3.3 Microcell Assembly

Components of the optics board were connected to each another using screws (6.2mm, M6 tapped) and the corresponding hex key, alternate screws were tightened to avoid uneven stressors. A firm grip of both hooks was maintained when unsecuring elastic cords to prevent any damage or injury in case of an accidental and sudden release.

The microcell base was assembled by mounting a fiber optic gooseneck to the back edge of the base and was connected to a light source so that the testing area could be illuminated. The support column was screwed into the base center, X/Y coarse adjusts were mounted perpendicular to one another in front of the support column and X/Y fine adjusts were mounted on top in a similar fashion. Base screws were put on both sides and a magnifying lens was mounted to the one side of the X/Y adjusts (Fig 11).

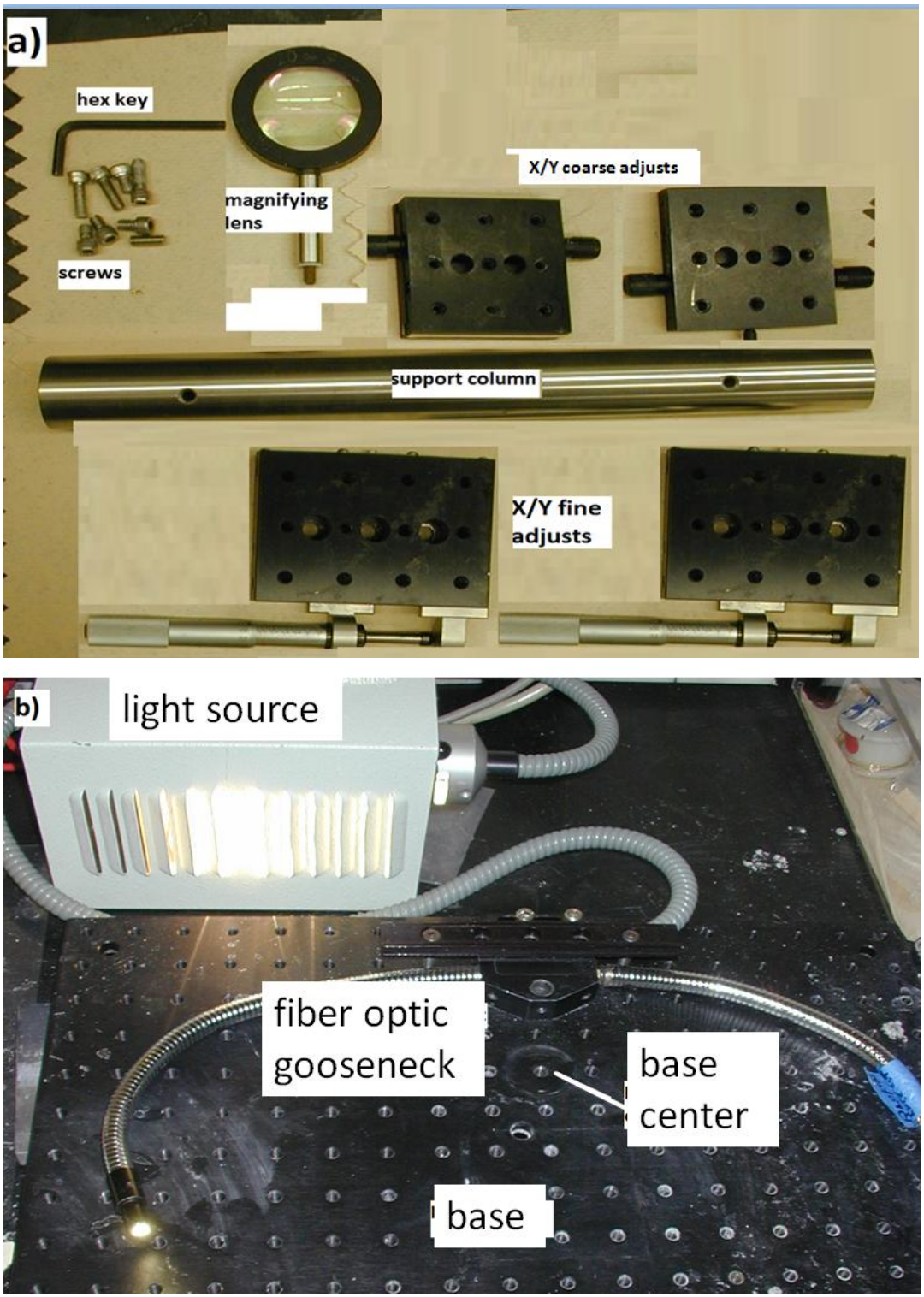

Figure 11: Parts used for assembly of microcell base (a), a fiber optic light was used to illuminate the testing area (b).

The tapped hole of the sample was filled with pieces of aluminum foil and then screwed with a threaded metal rod. The electrical connection between the sample surface and rod was verified

without damaging the polished surface and was tightened using pliers if necessary. The sample stage was mounted on top of the X/Y fine adjusts using screws and washers, the sample was screwed into the correct hole size with a rubber disk in-between and aligned parallel to X/Y gridlines. A clip was attached to the threaded rod below the sample stage for an electrical connection and a tissue was placed in between to prevent unnecessary movements during testing (Fig 12).

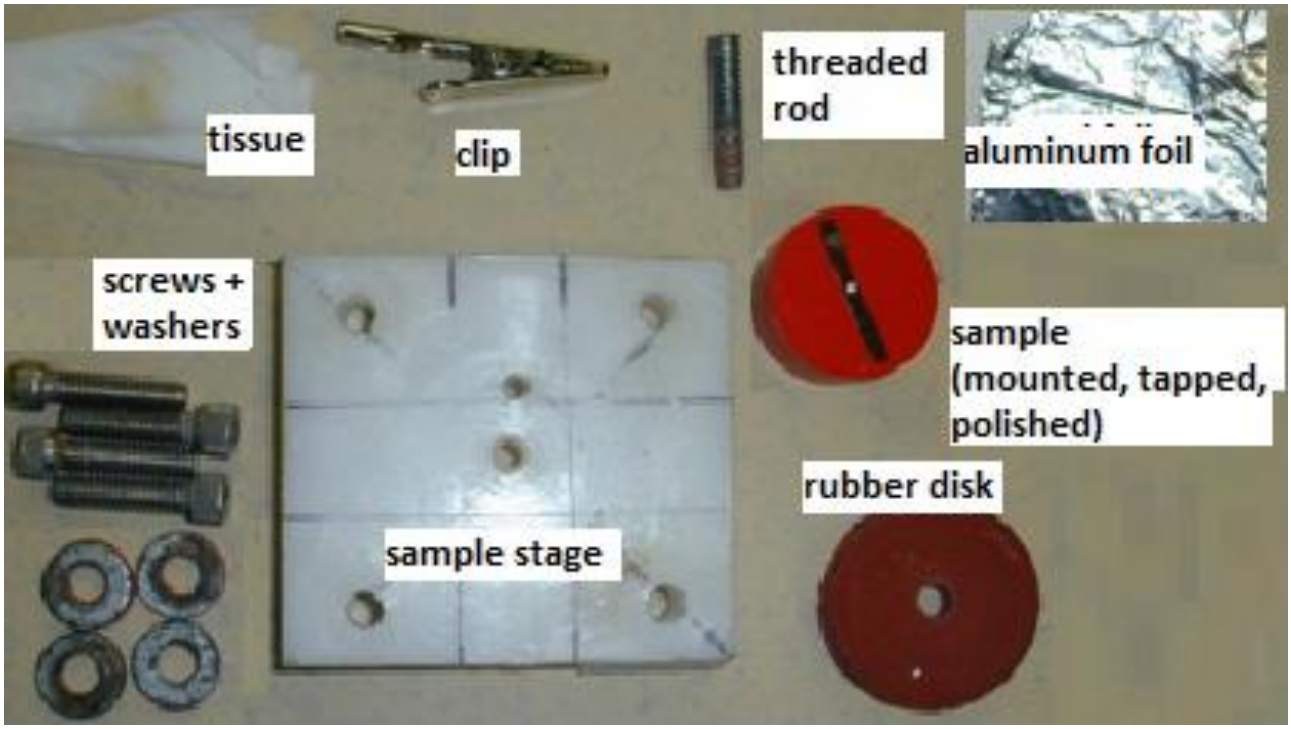

Figure 12: Parts used for assembly of the sample stage that would provide a secure connection to leads from the potentiostat and a keep the sample surface parallel to the X/Y plane.

A spacer was placed on top of the sample with arrow pointing outwards, the Z-fine adjust was mounted to the Z-clamp. This was adjusted onto the support column so that the long screws rested just above the spacer. The bottom support was placed on the long screws and the back support was placed on the face of the Z-fine adjust. The capillary was fit into its corresponding port on the microcell cube using an O-ring and fastener. The microcell cube was fit into the right angle formed between the bottom and back supports (Fig 10b) so that the capillary could fit through the hole of the bottom support and the port X could face outwards. Cord A was secured over the microcell cube and hooked onto the base screws preventing any damage to the cube in case of an accidental and sudden release. Both cord B's were put around the CE and inlet (side) ports to secure the microcell cube. Cord A was unsecured and removed to make room for

securing both cord C's around the side ports and hooking to the long screws. The Z-clamp was readjusted to a higher position on the support column so that the Z-fine adjust could be adjusted to a setpoint value of 10 mm, the Z-clamp was adjusted to a final position so that the bottom support rested on top of the spacer. The inlet tube (male end), CE and rubber disk were fitted into their corresponding ports on the microcell block using fasteners, rubber O-ring and ferrule. The Z-fine adjust was raised so that the spacer could be removed, and then it was lowered to compress the capillary sealing on the metal surface. The microcell cavity was slowly filled with test solution using the 20 mL syringe and needle through the top RE port while holding the female end of the inlet tube the same height as the RE top port. The 1.0 mL syringe was attached to this female end once test solution came out of it and the remainder of the microcell cavity was filled with test solution. Light was shined through the inlet tube and microcell cavity to verify the absence of bubbles; any remaining bubbles are purged if necessary. The RE was removed from its vial of saturated KCl and fit into the top port using an O-ring and fastener. The Z-fine adjust was raised to create a 2 centimeter separation between the capillary tip and sample surface. Test solution was forced thru the capillary tip into a test tube held below at a 45^{o} angle and bubble control at the capillary tip was verified using the 1.0 mL syringe (Fig 10b, 13).

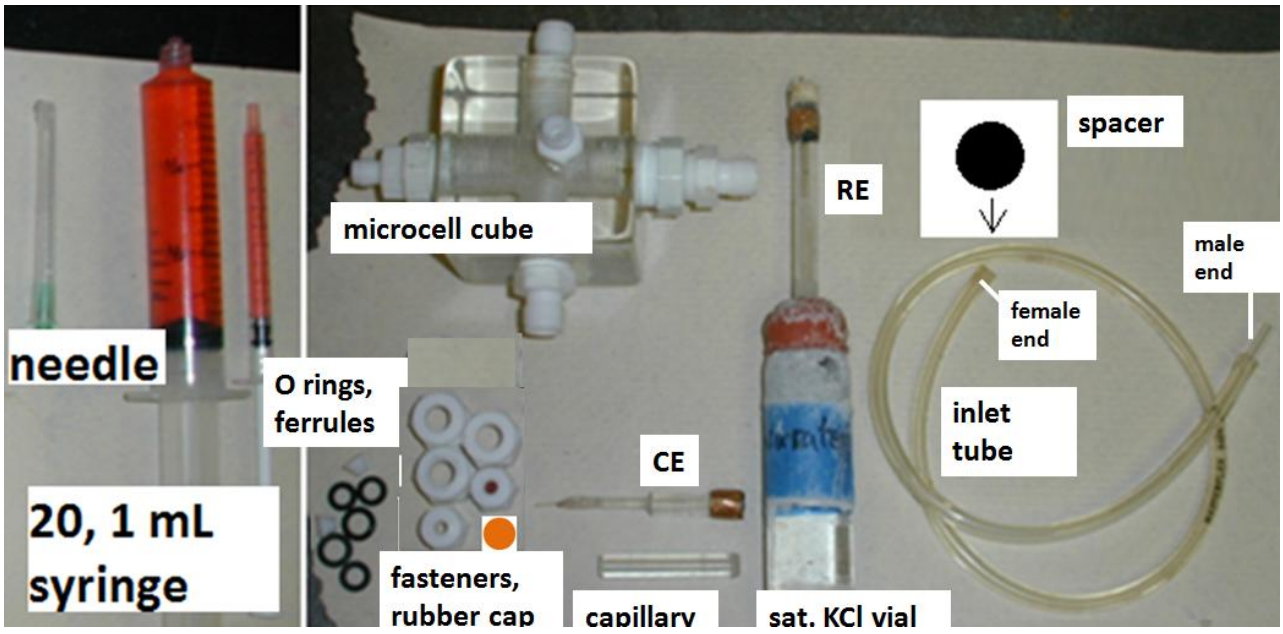

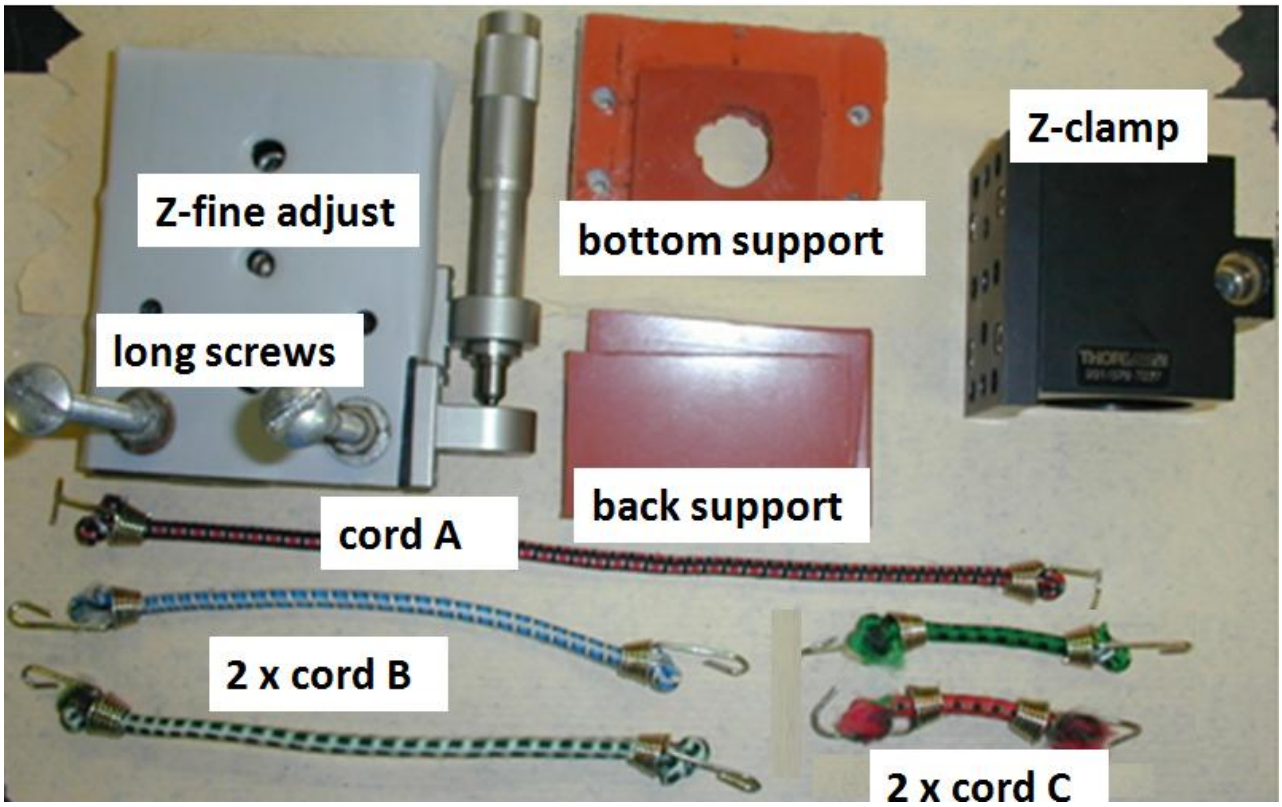

Figure 13: Parts used for assembly of the microcell cube.

3.4 Spot Test Procedure

After powering on the computer and potentiostat the corresponding leads were connected to the CE, RE and WE (sample); all electrical connections were verified. The X/Y course adjusts were moved so that the capillary could be positioned anywhere on the sample surface using only X/Y fine adjusts and the sample mount was marked indicating location of the initial spot test. Prior to each polarization (spot) test the solution bubble at the capillary tip was verified using the magnifying lens, the Z-fine adjust was lowered to compress the capillary sealing onto the sample surface and OCP versus time was measured. The setpoint value on the Z-fine adjust was used to estimate how much further the capillary sealing needed to be compressed on the sample surface for the most stable OCP reading. In the case of an unstable OCP the RE was removed from its port, refilled with saturated KCl to eliminate bubbles before comparing its stability to a standard RE. After completing each spot test the Z-fine adjust was raised and the X/Y fine adjusts were used to move the sample in regular increments parallel to the XY plane.

3.5 Microcell Disassembly

After completing all spot tests the potentiostat and computer were turned off, corresponding leads to the CE, RE and WE were disconnected and the cable was stored. The Z-fine adjust was raised to create a 2 cm separation between the capillary tip and sample surface, and the 1.0 mL syringe was depressed so that test solution could drain into a test tube is held at a 45^{o} angle below. The inlet tube (male end), CE, RE and rubber cap were removed from their corresponding ports. The RE was stored in a vial of saturated KCl to prevent unwanted crystal growth at the vycor frit. The spacer was placed upon the sample surface before lowering Z-fine adjust so that the bottom support could rest upon on the spacer. Both cord C's were unsecured and removed so that cord A could be secured over the microcell cube and hooked onto the base screws preventing possible to damage (see *3.3 Microcell Assembly*). After unsecuring and removing both cord B's cord A was carefully unsecured and removed so that the microcell cube, bottom and back supports could be removed. The capillary was removed from the microcell cube before the microcell cavity and inlet tubes were rinsed with deonized (DI) water and blown with compressed air.

CHAPTER 4 MATERIALS AND METHODS

Samples were prepared in which microstructure differed in macroscopic regions allowing the utility of the microcell to be assessed by detecting (localized) corrosion based on region of spot test.

4.1 Sample Preparation

A 3 mm thick sheet of type 304 stainless steel (Table 2) purchased from Metal Samples was cut and welded using a metal inert gas (MIG) technique with 316L as the filler metal. An abrasive cutter was used to section rectangular samples (3.0 cm x 0.5 cm) of the 304 weld. Etching in 10 second intervals using 10 % weight oxalic acid and 6 V (Fig 14a) revealed distinct regions of the weld profile: weld, heat-affected zone (HAZ) and base metal.

Table 2: Chemical compositions (by weight %) of 304 and 316L stainless steels were determined by energy dispersive X-rays; remaining compositions are assumed to be iron.

SS Alloy	Cr	Ni	Mn	Si	Mo	N	C	P	S
304	18.2	8.12	1.50	0.342	0.103	0.0524	0.0328	0.0325	0.0022

316L	18.5	12.0	1.00	0.300	2.50	0.0500	0.0300	0.0400	0.00200

A 2 cm diameter rod of carburizable stainless steel 42L (CSS 42L) (Table 3) was carburized at 954^{o}C, austenized at 1121^{o}C and then oil quenched [3]. A wedge sample was sectioned normal to its axis so that layers of distinct microstructures could be revealed.

Table 3: Weight % composition of CSS 42L; the remaining composition is assumed to be iron [3].

Cr	**Co**	**Mo**	**Ni**	**V**	**C**	**Cb**
14.0	12.5	4.75	2.00	0.60	0.12	0.02

A 7.0 cm x 1.0 cm profile was sectioned perpendicular to the weld direction of a friction-stir welded aluminum (FSW Al 2195) bar that was previously cast and extruded. Spot tests demonstrated how the microcell technique can be used to relate microstructure and localized corrosion on any passive metal surface susceptible to localized corrosion in chloride environments. No filler metal was added so that composition remained constant (Table 4) and only microstructure varied throughout the weld profile. Etching in Kellers Reagent revealed the distinct microstructures of five regions: stir zone (SZ), thermo-mechanically affected zone (TMAZ), heat-affected zone (HAZ) and base metal.

Table 4: Weight % composition of FSW Al 2195 assumed to remain constant throughout weld profile [28].

Al	Cu	Li	Mg	Ag	Zr
93.4	4.00	1.00	0.525	0.425	0.120

Stainless steel samples were hot mounted in a phenolic resin using an Allied High Tech mounting press, the FSW Al 2195 sample was not mounted. A hole was drilled and tapped through the bottom of each sample for electrical connection and attachment to the sample stage. Samples were polished to a 0.05 micron finish using SiC, diamond and alumina abrasive particles purchased from Precision Surfaces International.

4.2 Bulk and Spot Testing

An EG&G potentiostat (Model 263A) was used measure OCP and perform all cyclic polarization experiments starting 1 V below OCP and using a 5 mV/sec scan rate. The point of scan reversal was chosen to be two orders of magnitude greater that the passive current. A standard RE (Corning 476406) was used to determine stability of the fabricated RE, a stable

OCP was determined to be 1 mV/sec or less. Bulk polarization tests were completed in 100 mL of test solution using the setup shown below (Fig 14b), platinum was used as the CE to support a greater exchange current for a greater WE area.

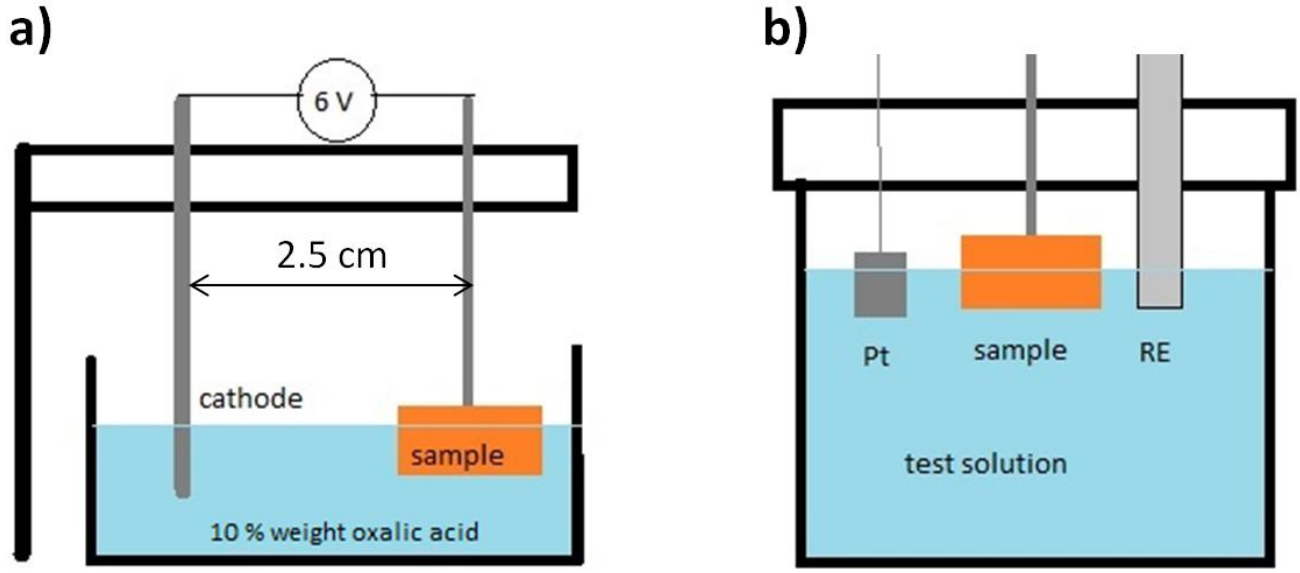

Figure 14: 304 weld samples were etched using 6 V, 10 % weight oxalic acid and a 2.5 cm separation between anode (sample) and cathode (noble metal). Bulk polarization setup (b) showing counter (Pt), working (sample) and reference electrodes submerged in test solution.

Consecutive spot tests beginning at a marked edge were done in regular increments across the surface of each sample using the developed microcell (see *3.4 Spot Test Procedure*). An optical microscope (Nikon 144745), camera (Clemex 50117) and Image J analysis software were used to determine the surrounding microstructure and estimate area of each spot. Four test solutions (Table 5) were used for spot and bulk testing 304 Weld samples so that pH and chloride effects could be determined. These were prepared using NaCl and KOH (JT Baker) and an analytical balance (Denver Instruments), a pH electrode (Thermo Scientific Orion, 9156BNWP) was used to confirm acidities, and 1 M NaCl was used for spot testing CSS 42L and FSW Al 2195 samples.

Table 5: Test solutions used for bulk and spot testing so that the affects of acidity (pH) and chloride concentration [Cl^-] could be determined.

		pH	
		7	**11**
[Cl-]	**1.0**	N0	B0
	0.1	N1	B1

CHAPTER 5 RESULTS AND DISCUSSION

Polarization data was plotted and values were computed using Microsoft Excel 2007, current densities were determined by normalizing measured current to the estimated area. OCP values were determined to be 1 V greater than the lowest potential value. Pitting potentials were determined qualitatively to be the onset of abrupt increases in current density (1 decade/0.1 V or greater) during the forward anodic scan followed by a loop hysteresis after reversal. Charge densities for hysteresis loops were determined using (Eq 5) where times t1 and t2 correspond to the pitting and repassivation potentials respectively.

5.1 304 Weld

A quantitative comparison of charge densities for hysteresis loops could not be determined because repassivation potentials were not reached for all spot tests (Fig 15). However a qualitative comparison reveals that the hysteresis size increased with greater pitting potentials. Bulk tests show lower OCP and pitting potentials compared to spot tests (Fig 16a) indicating occurrence of crevice corrosion between the sample and thermoplastic mount. A general trend of pitting potentials (Fig 16b) indicates that corrosiveness increased in the order of: N0, B0, B1 and N1 test solutions confirming that greater acidity and chloride content increases localized attack. Pitting potentials decreased in the order of weld, base and HAZ regions for all test solutions. These results confirm that greater amounts of chromium and nickel content increase resistance to localized attack, and sensitization in the HAZ decrease resistance to localized attack. Oxalic acid etching did not reveal any difference in microstructure between the HAZ and base regions (Fig 17a-b) indicating another etchant is needed to reveal subtle differences in sensitization and grain structure.

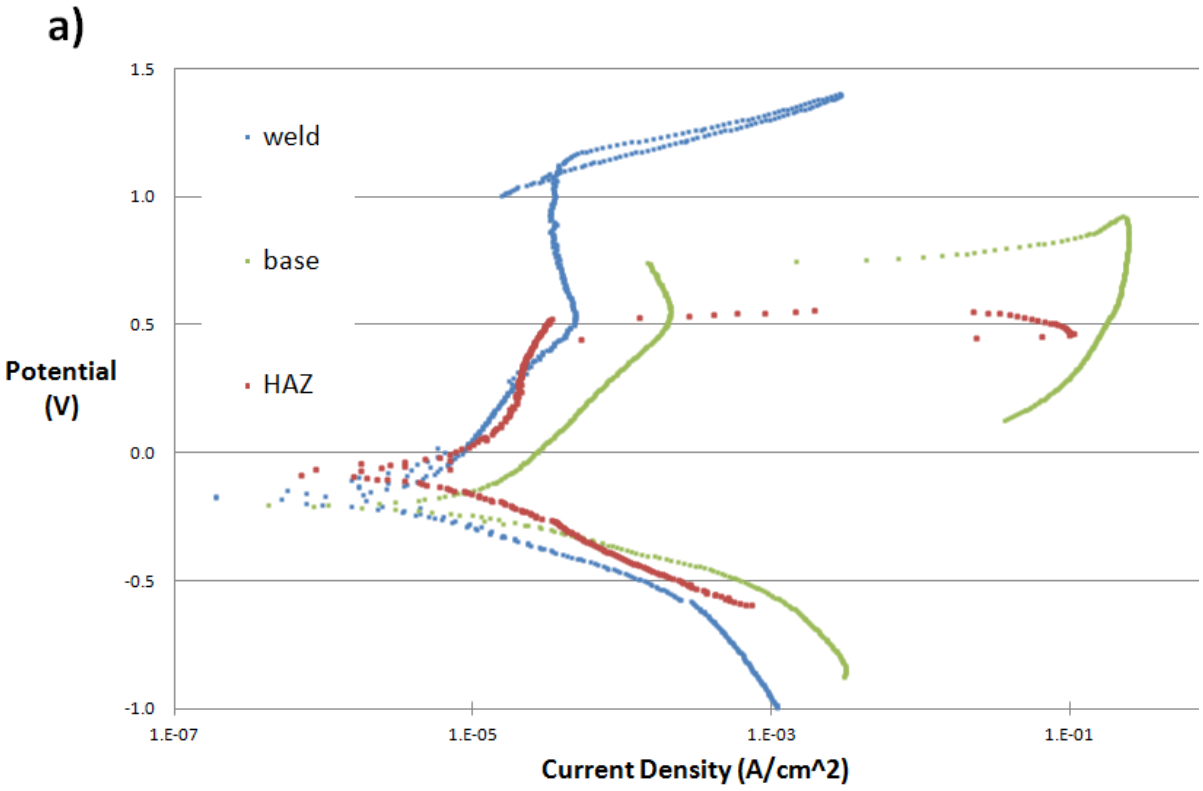
a)
1.5
1.0
0.5
0.0
-0.5
-1.0
weld
base
HAZ
Potential (V)
1.E-07
1.E-05
1.E-03
1.E-01
Current Density (A/cm^2)

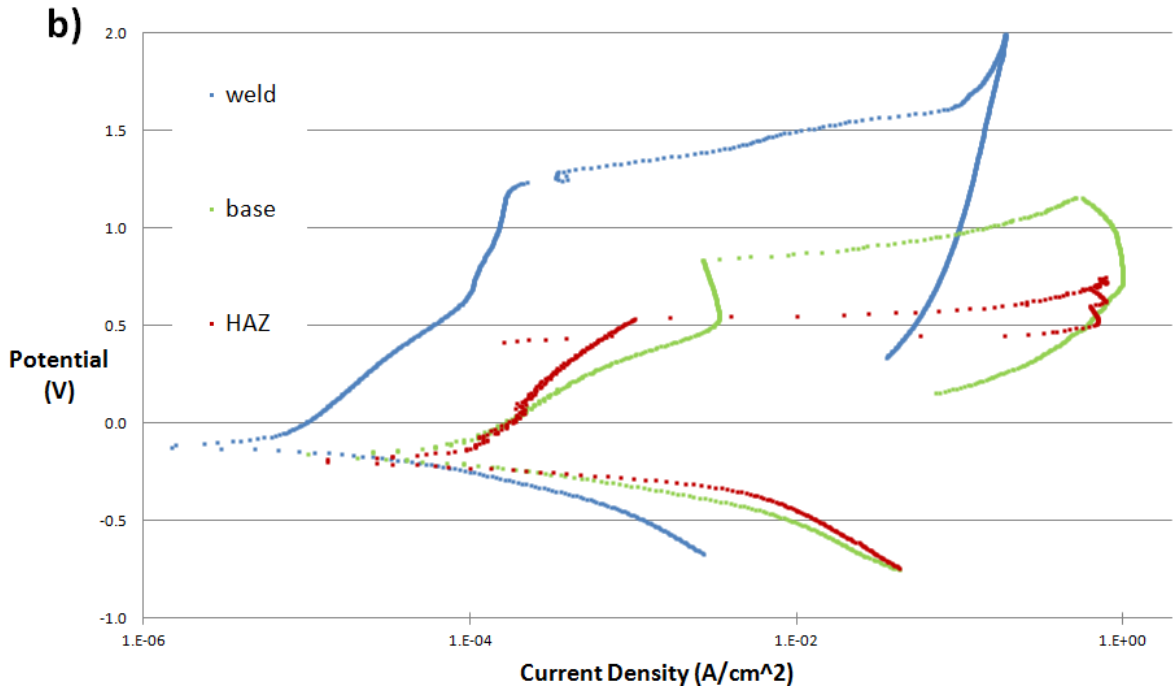
b)
2.0
1.5
1.0
0.5
0.0
-0.5
-1.0
weld
base
HAZ
Potential (V)
1.E-06
1.E-04
1.E-02
1.E+00
Current Density (A/cm^2)

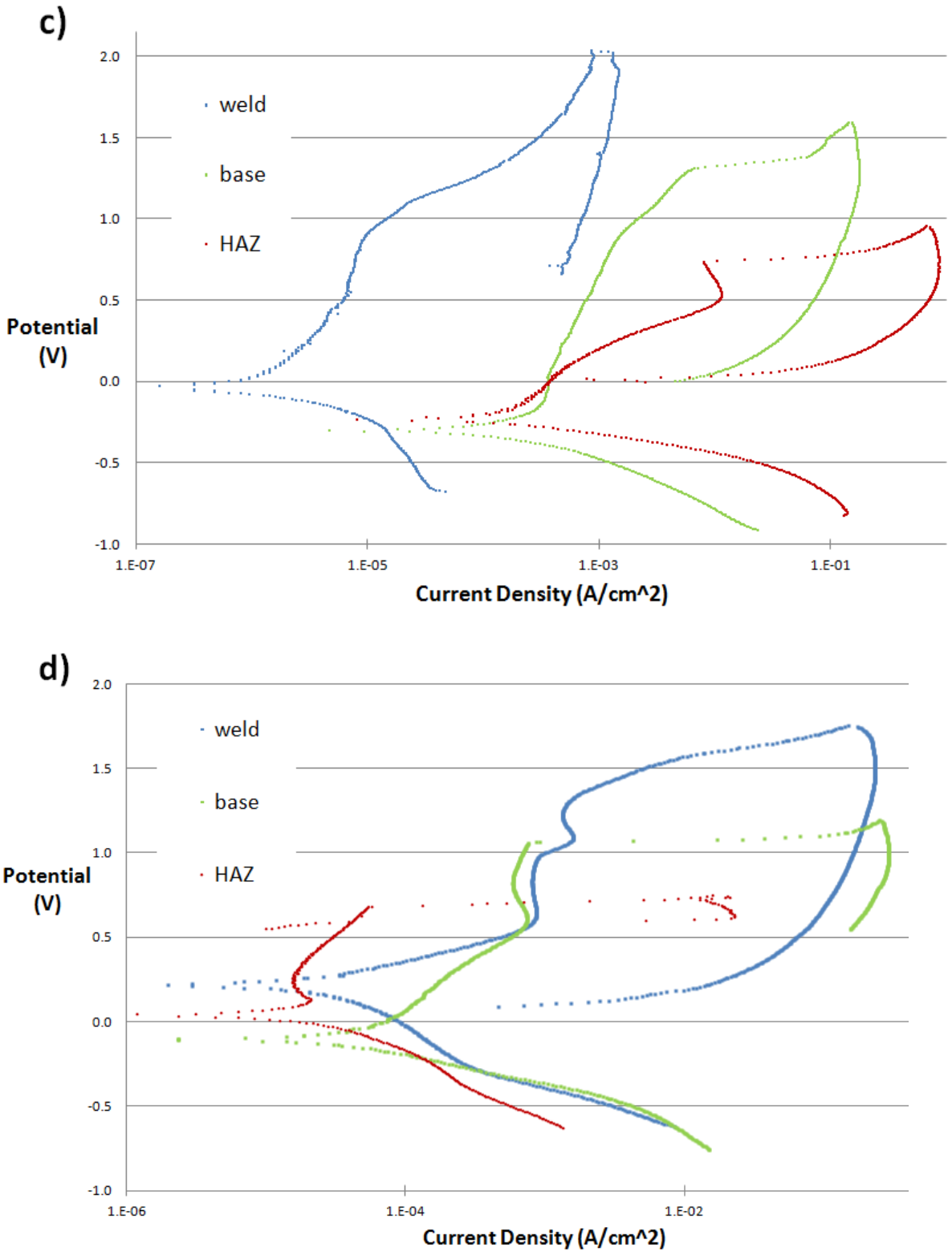

Figure 15: Cyclic polarization data of spot tested 304 Weld samples for each test solution: N0 (a), B0 (b), N1 (c) and B1 (d).

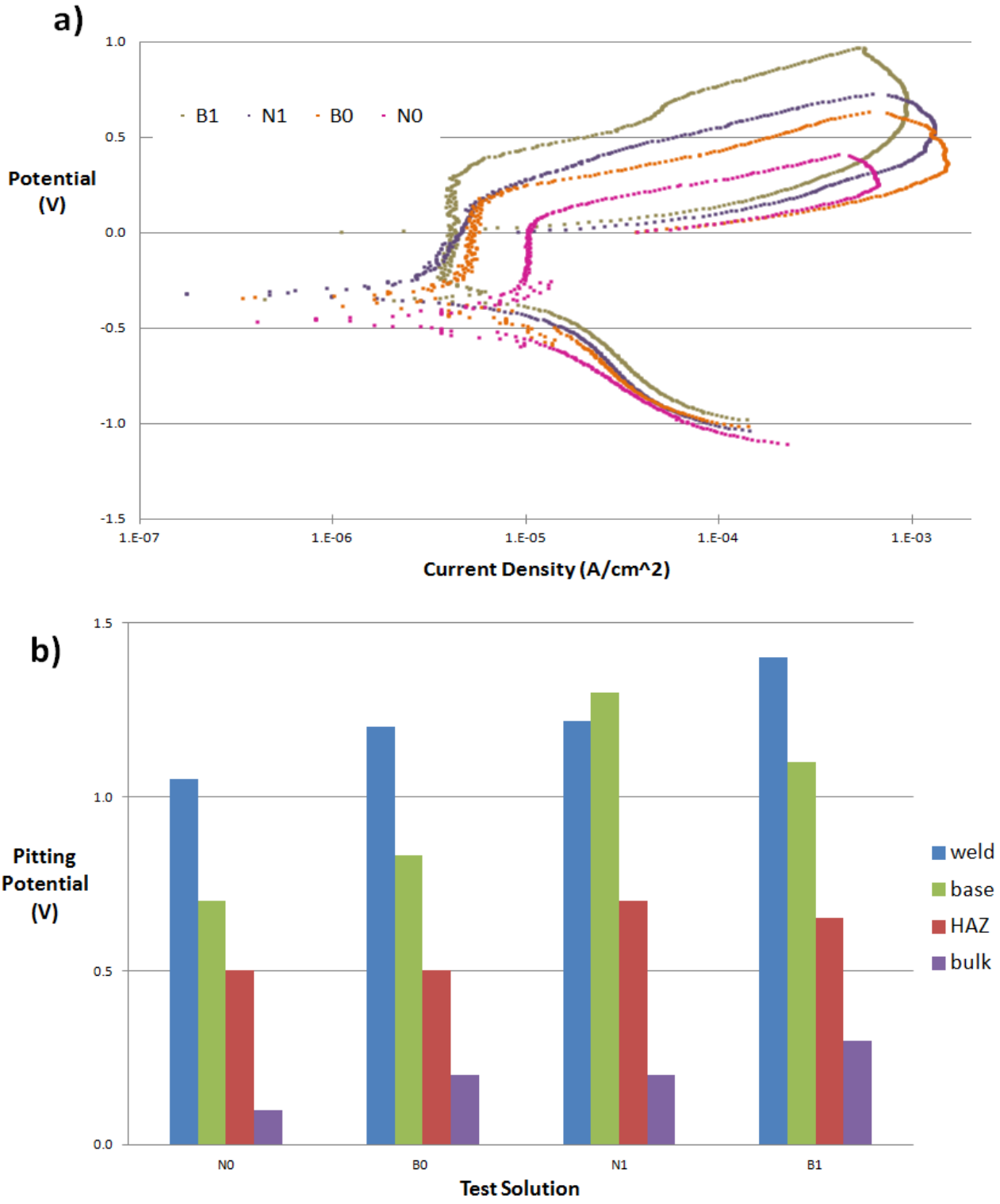

Figure 16: Cyclic polarization data of bulk tested 304 Weld samples preformed in each test solution (a), pitting potentials for spot and bulk tests (b) observed for each test solution.

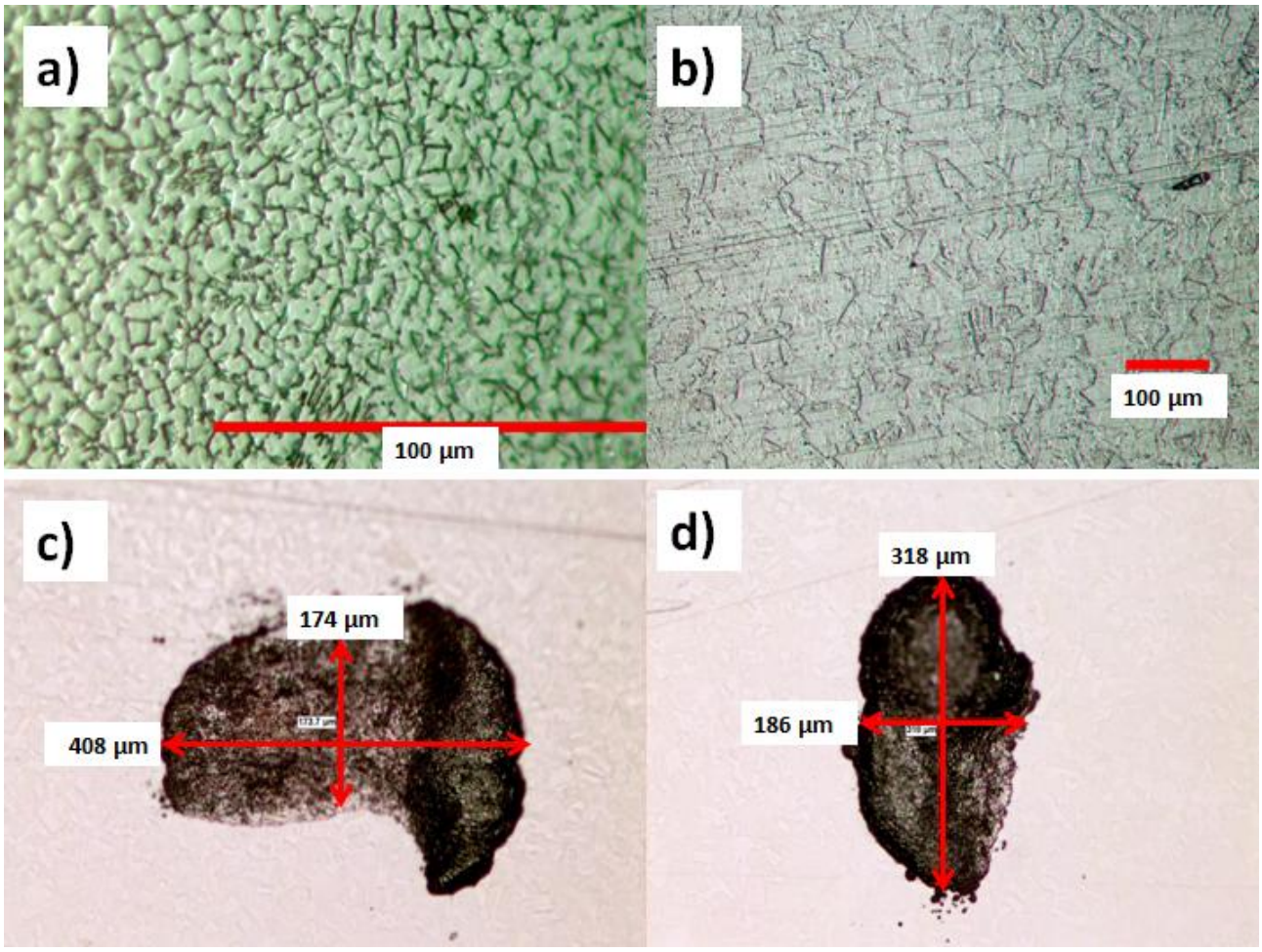

Figure 17: Microstructures of the 304 Weld profiles showing dendrite formation in the weld region (a) and twinning of grain structure in the base metal (b), no differences were observed between HAZ and base regions of the 304 Weld using oxalic acid etching. Image J software was used to estimate the area of each tested spot (c-d) based dark/light contrasts.

5.2 CSS 42L

Charge densities for hysteresis loops (Table 6, Fig 19) could not be converted to mass reacted per unit area used because of compositional gradients across the macrostructure. Pitting potentials and charge densities increased with increasing distance from the edge indicating that the microstructure of austenite with chromium carbides was most susceptible and martensite was least susceptible to localized attack. No trends were observed for average passivation current densities ($<i_{pass}>$) during the forward anodic scan.

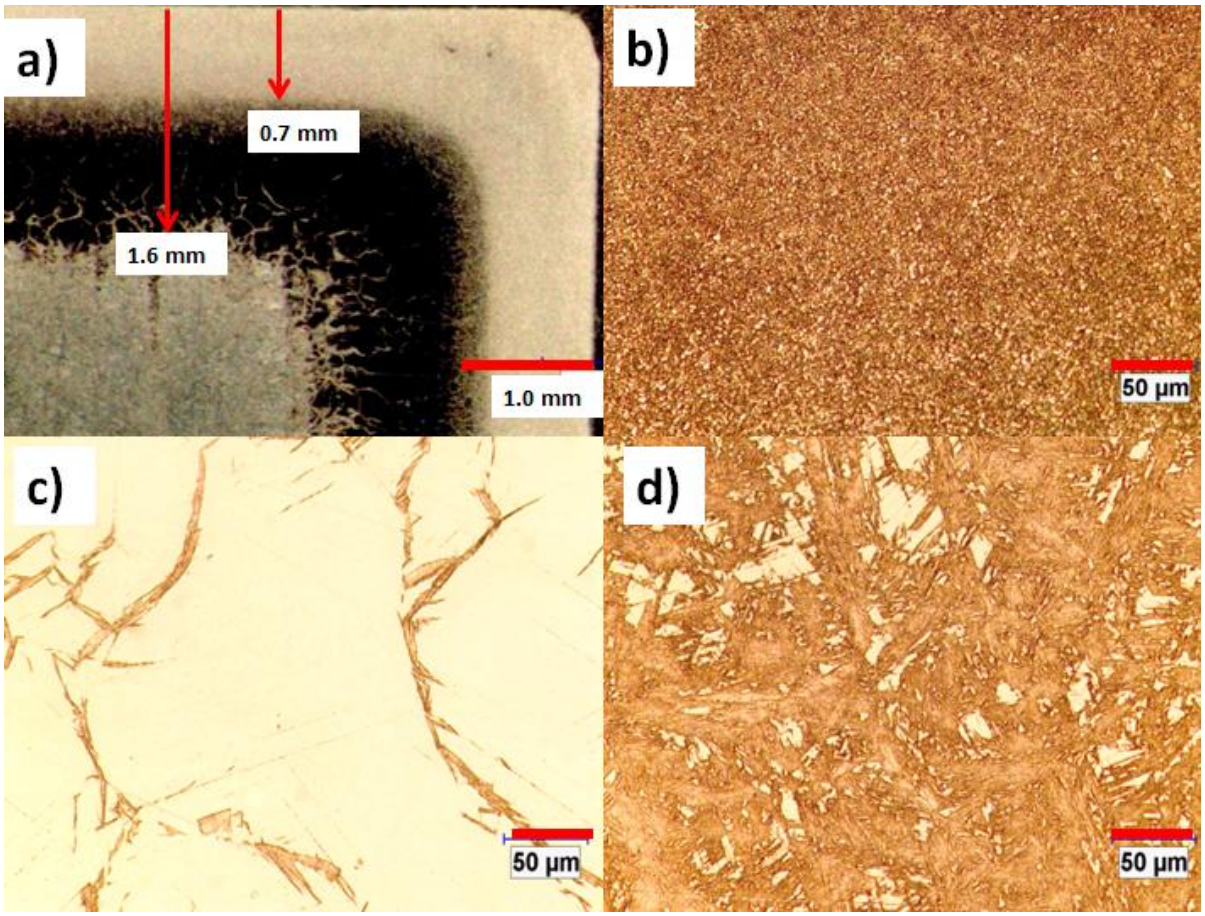

Figure 18: Cross-section of CSS 42L (a) showing distinct microstructural regions as a function of distance from the edge: austenite and chromium carbides less than 0.7 mm (b), austenite and martensite between 0.7 and 1.6 mm (c), and martensite greater than 1.6 mm (d).

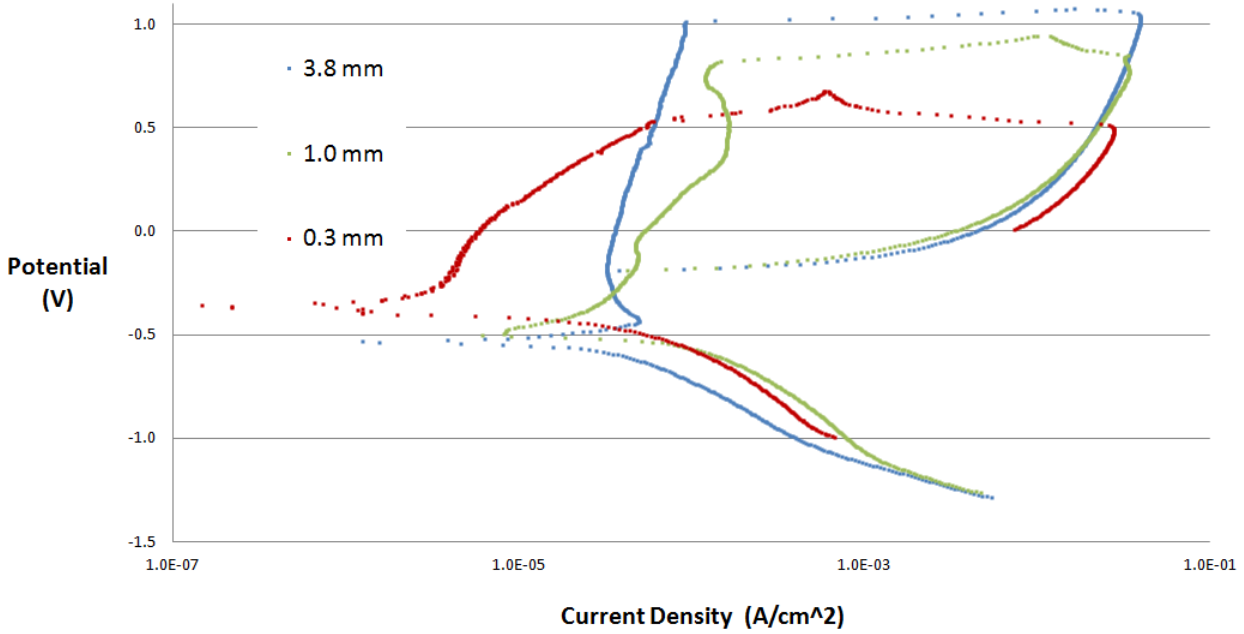

Figure 19: Cyclic polarization data of spot tested CSS 42L using 1M NaCl test solution

Table 6: Pitting potentials and passivation current densities were determined qualitatively from cyclic polarization data of spot tested CSS 42L using 1 M NaCl test solution, charge densities for hysteresis loops were found using (Eq 5).

microstructure	distance from edge (mm)	pitting potential (V)	<i_{pass} (A/cm^2)>	Q (C/cm^2)
martensite	3.8 mm	1.00	5.19E-05	5.14
Austenite + martensite	1.0 mm	0.74	1.11E-04	3.80
Austenite + chromium carbides	0.3 mm	0.49	1.41E-05	2.02

5.3 FSW Al 2195

Masses reacted per area for hysteresis loops (Fig 20, Table 7) were found using (Eq 5-7) and known alloy compositions (Table 4). SZ showed the greatest OCP value indicating that the small, equiaxed grain microstructure had the least thermodynamic tendency to corrode. TMAZ showed the greatest passivation range indicating that the plastically deformed microstructure with few second phases developed an effective passive film. The base metal had the least OCP value and no passivation range indicating that as-cast, extruded microstructure with few second phases had the greatest thermodynamic tendency to corrode and did not form an effective passive film. Spot tests in the HAZ microstructure containing the greatest amount of sensitization did not show any distinct values.

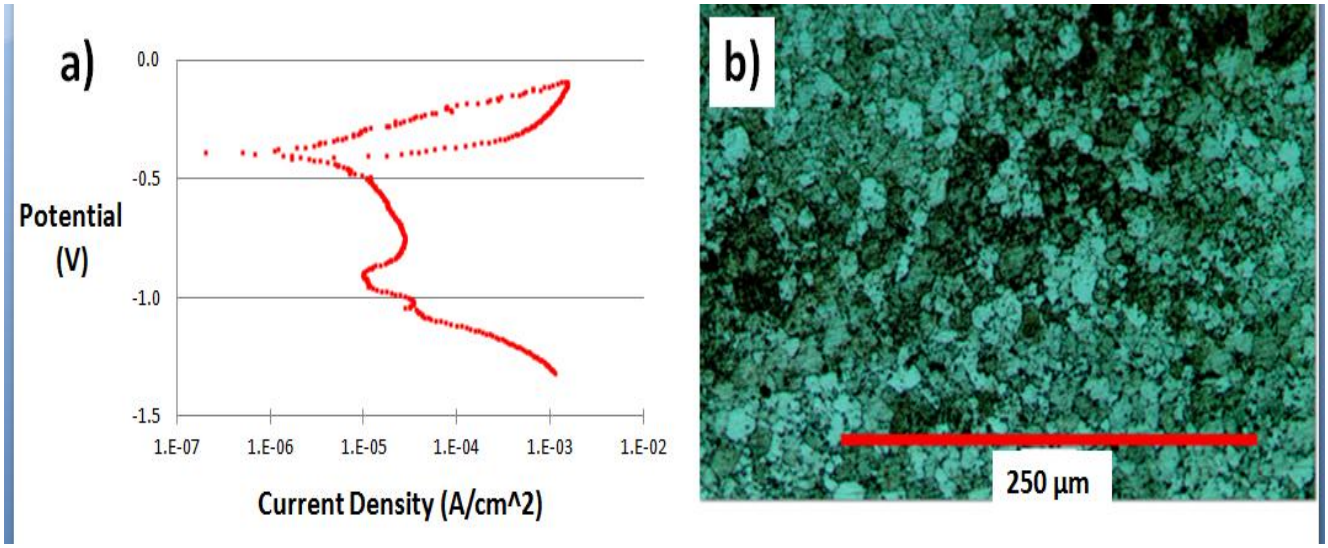

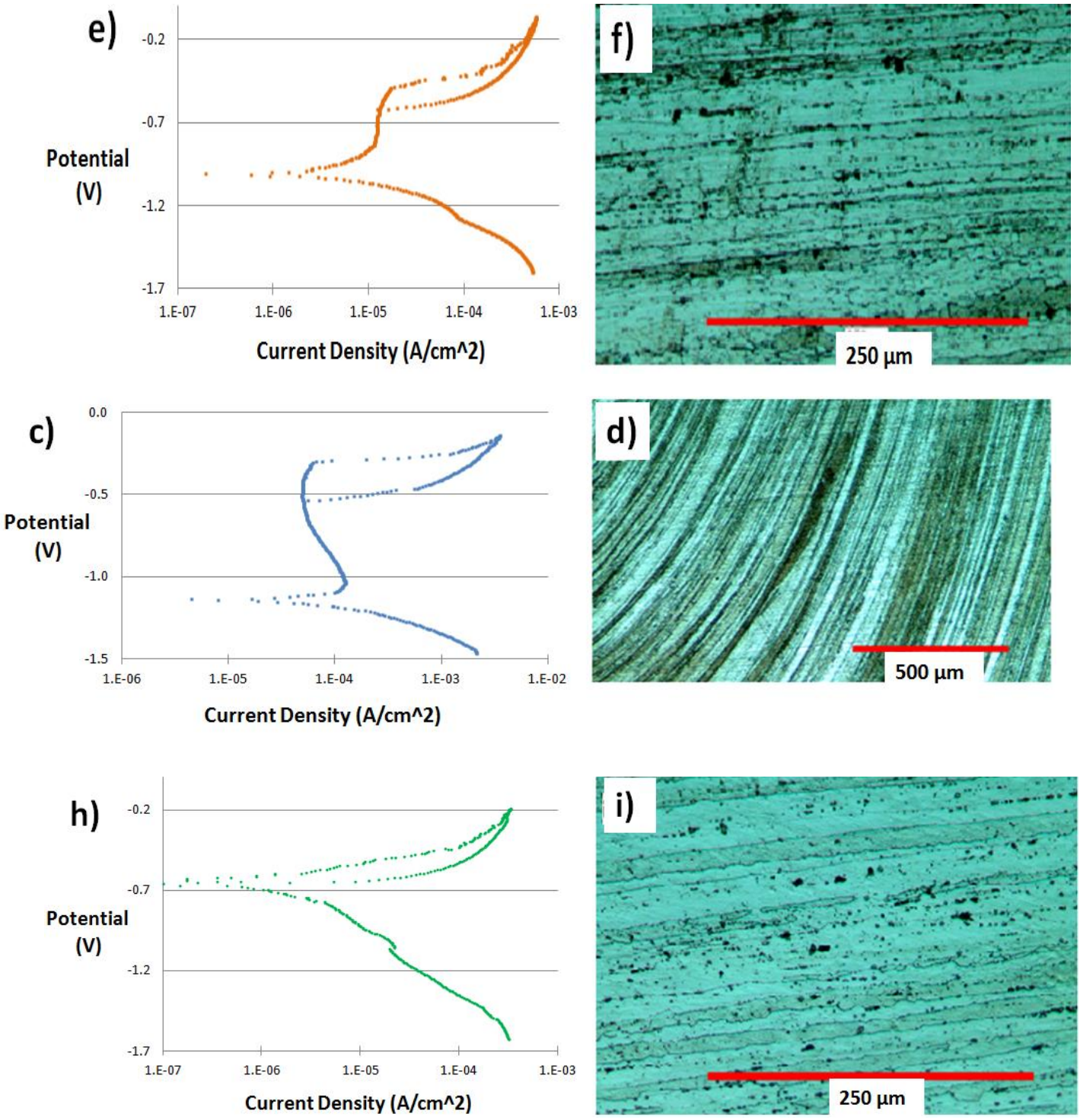

Figure 20: Cyclic polarization data and corresponding microstructures for spot tested FSW Al 2195 using 1 M NaCl: SZ (a-b), TMAZ (c-d), HAZ (e-f) and base (h-i).

Table 7: OCP, passivation and pitting potentials were determined qualitatively from cyclic polarization data of spot tested FSW Al 2195 for each microstructural region, passivation range was determined to be the difference between pitting and passivation potentials. Mass reacted per area (m) was found using (Eq 5-7).

Weld region	OCP (V)	Passivation Range (V)	m (g/cm^2)
SZ	-0.319	0.35	6.64E-06
TMAZ	-0.469	0.72	1.96E-05
HAZ	-0.607	0.32	6.23E-06
base	-0.632	NA	2.86E-06

CHAPTER 6 CONCLUSION

Sensitized austenitic microstructures confirm greater susceptibility to localized attack based on spot tests across 304 Weld and CSS 42L profiles. Greater amounts of nickel and chromium confirm more noble pitting potentials based on spot tests across 304 Weld profiles and a comparison of spot tested 304 Weld and CSS 42L samples. Comparison of bulk and spot test data of 304 Welds demonstrates the utility of the developed microcell by confining electrochemical activity on the metal surface to areas less than 1 mm^2. Spot tests of FSW Al 2195 further demonstrate how the microcell can be used to determine microstructure-property relationships for any passive metal surface susceptible to localized chloride attack. A reduced scan rate will allow determination of activation energies and reaction kinetics using Tafel extrapolations. Adjusting test parameters so that repassivation potentials can be reached will allow quantitative comparisons of how charge density for hysteresis loop changes with acidity and chloride content.

CHAPTER 7 FUTURE WORK

This microcell will be further refined to spot test areas less than 1000 μm^2 and reveal polarization behavior of distinct microstructural features.

7.1 Microcapillary Sealing & Fitting

A sealing will be created using PDMS at the polished end of a microcapillary less than 50 microns in diameter (Fig 21a) based on a technique developed by Suter and Bohni [26]. This will be practiced on 1 mm diameter tips before graduating to smaller sizes. The microcapillary shaft

will be encapsulated into plastic (Fig 21b) so it can be fitted into the capillary port of the microcell cube and tested.

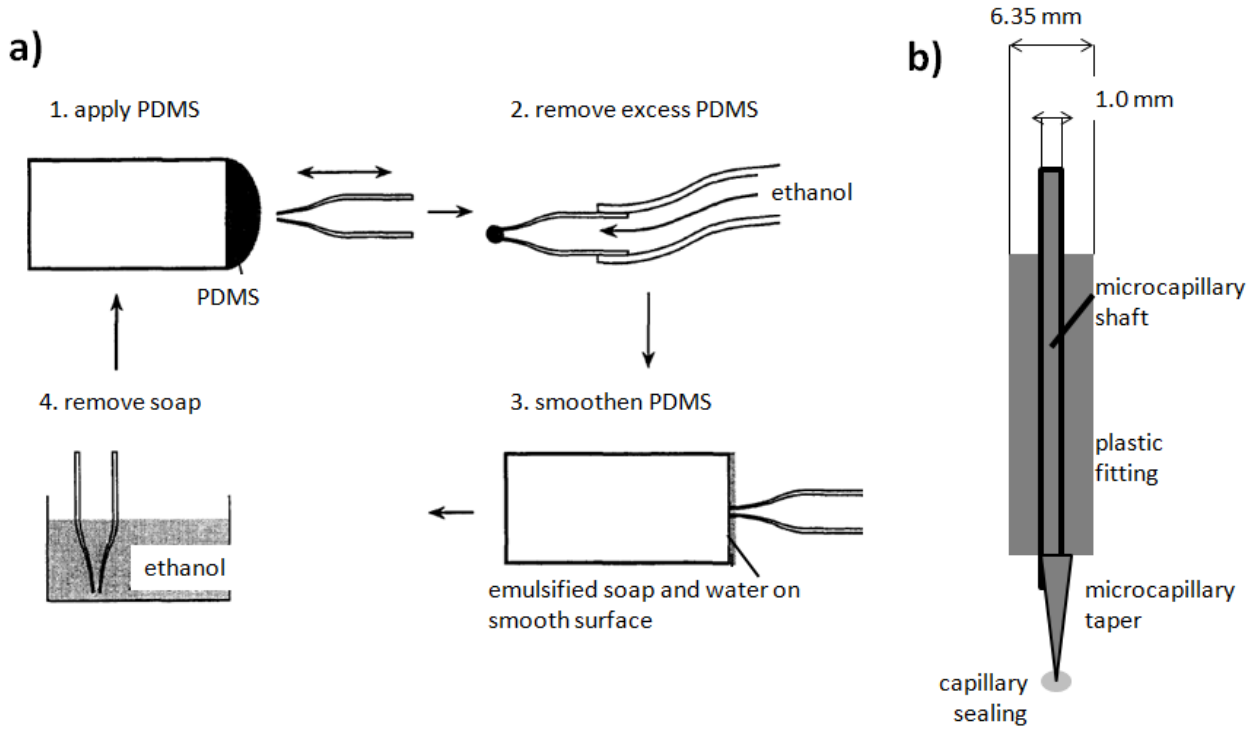

Figure 21: Creating a microcapillary sealing (a) consists of four steps: apply thin layer of PDMS, force ethanol through to remove excess PDMS and create hole, gently rub PDMS on a smooth surface covered with emulsified soap and water to smoothen it and soak in ethanol to remove soap [26]. This process is repeated several times until a microcapillary sealing of appropriate thickness is created, the microcapillary shaft will be encapsulated into plastic so it can be fitted into the capillary port of the microcell cube.

7.2 Reference Electrode for FGE

The RE for testing in fuel grade ethanol (FGE) [see proposal] will be fabricated from an Ag/AgCl wire in ethanol saturated with LiCl similar to the previous RE design (Fig 8b). The extendable design will allow the RE to be placed near the capillary to compensate for the high resistivity of FGE [29].

References

[1] M. Genet, Orban, C., "Steel, Alloys and Stainless: Part II," in *Stainless Steel World*, Beaune, France, October 13, 2010.

[2] A. J. Sedriks, *Corrosion of stainless steels*, 2nd ed. ed. New York :: Wiley, 1996.

[3] e. a. Maloney, "Case Carburized Stainless Steel Alloy for High Temperature Applications," USA Patent, 1995.

[4] R. D. Moser, "High-Strength Stainless Steels for Corrosion Mitigation in Prestressed Concrete: Development and Evaluation," Ph.D. dissertation, School of Civil and Environmental Engineering, Georgia Institute of Technology, Atlanta, GA, 2011.

[5] G. H. B. Koch, Michiel P.H.; Thompson, Neil G.; Virmani, Y. Paul; Payer Joe H., "Corrosion Cost and Preventive Strategies in the United States," O. o. I. R. a. Development, Ed., ed. McLean, VA, September 30, 2001, pp. 1-82.

[6] J. A. B. Sederholm, and S. Randström "Corrosion Properties of Stainless Steels as Reinforcement in Concrete Swedish Outdoor Environment," presented at the Corrosion 2009: Conference & Expo, Atlanta, GA, 2009.

[7] J. R. S. F.M. Moreno, S.R. Sharp, "Literature Review of Commercially Available Alloys that Have Potential as Low-Cost Corrosion Resistant Concrete Reinforcement," presented at the Corrosion 2009: Conference & Expo, Atlanta, GA, 2009.

[8] W. H. Hart, "Performance of Corrosion Resistant Reinforcements In Concrete and Application of Results to Service Life Projection," presented at the Corrosion 2009: Conference & Expo, Atlanta, GA, 2009.

[9] P. K. Mehta, *Concrete : microstructure, properties, and materials*, 2nd ed. ed. Englewood Cliffs, N.J. :: Prentice Hall, 1993.

[10] S. N. S. M. Wigen, "Corrosion Problems and Corrosion Mitigation Experiences on 6Mo Stainless Steel Seawater Systems on the Sleipner Platforms - North Sea," presented at the Corrosion 2008: Conference & Expo, New Orleans, LA, 2008.

[11] M. S.-T. A. Okeremi, "External Pitting and Crevice Corrosion of 316L Stainless Steel Instrument Tubing in Marine Environments and Proposed Solution," presented at the Corrosion 2008: Conference & Expo, New Orleans, LA, 2008.

[12] J. P. T. Havn, "Developments of Materials and Design for Mitigation of Marine Corrosion Topside," presented at the Corrosion 2000, Orlando, FL, 2000.

[13] U. Steinsmo, T. Rogne, and J. Drugli, "Aspects of Testing and Selecting Stainless Steels for Seawater Applications," *CORROSION,* vol. 53, pp. 955-964, 1997.

[14] D. A. Jones, *Principles and prevention of corrosion*, 2nd ed. ed. Englewood Cliffs, NJ :: Prentice Hall, 1996.

[15] P. Schmuki, "From Bacon to barriers: a review on the passivity of metals and alloys," *Journal of Solid State Electrochemistry,* vol. 6, pp. 145-164, 2002.

[16] A. International, "Standard Practice for Cleaning, Descaling, and Passivation of Stainless Steel Parts, Equipment, and Systems," ed, 2006.

[17] R. R. Maller, "Passivation of stainless steel," *Trends in Food Science & Technology,* vol. 18, pp. S112-S115, 2007.

[18] A. A. S. Jin, "ESCA-Studies of the Structure and Composition of the Passive Film Formed on Stainless Steels by Various Immersion Times in 0.1 M NaCl Solution," *Applied Physics,* vol. 42, pp. 149-165, 1987.

[19] X. Y. Wang, Y. S. Wu, L. Zhang, and Z. Y. Yu, "Atomic Force Microscopy and X-Ray Photoelectron Spectroscopy Study on the Passive Film for Type 316L Stainless Steel," *CORROSION*, vol. 57, pp. 540-546, 2001.
[20] Z. Szklarska-Smialowska, *Pitting corrosion of metals*. [Houston, Tex. :: National Association of Corrosion Engineers, 1986.
[21] A. A. Hermas, K. Ogura, S. Takagi, and T. Adachi, "Effects of Alloying Additions on Corrosion and Passivation Behaviors of Type 304 Stainless Steel," *CORROSION*, vol. 51, pp. 3-10, 1995.
[22] G. P. Halada, D. Kim, and C. R. Clayton, "Influence of Nitrogen on Electrochemical Passivation of High-Nickel Stainless Steels and Thin Molybdenum-Nickel Films," *CORROSION*, vol. 52, pp. 36-46, 1996.
[23] I. Olefjord and L. Wegrelius, "The influence of nitrogen on the passivation of stainless steels," *Corrosion Science*, vol. 38, pp. 1203-1220, 1996.
[24] Y. Fu, X. Q. Wu, E. H. Han, W. Ke, K. Yang, and Z. H. Jiang, "Effects of cold work and sensitization treatment on the corrosion resistance of high nitrogen stainless steel in chloride solutions," *Electrochimica Acta*, vol. 54, pp. 1618-1629, Feb 2009.
[25] D. H. v. d. W. J.H.W. de Wit, A.J. de Jong, F. Blekkenhorst, S.D. Meijers, "Local Measurements in Electrochemistry and Corrosion Technology," *Materials Science Forum*, vol. 289-292, pp. 69-76, 1998 1998.
[26] T. A. Suter, "Microelectrochemical Investigations of Austenitic Stainless Steels," PhD, Materials Science and Engineering, Swiss Federal Institute of Technology Zurich, Zurich, Switzerland, 1997.
[27] "Material Safety Data Sheet: Silicone Instant Gasket Maker-Clear," C-953 ed. Jupiter, FL 33477: Cyclo Industries Inc., 2012.
[28] (2012, May 1, 2012). *2105 Aluminum Composition Spec*.
[29] X. Lou and P. M. Singh, "Role of water, acetic acid and chloride on corrosion and pitting behaviour of carbon steel in fuel-grade ethanol," *Corrosion Science*, vol. 52, pp. 2303-2315, 2010.